Studying 2D materials with advanced Raman spectroscopy: CARS, SRS and TERS

Leandro M. Malard, [ID] * Lucas Lafeta, [ID] Renan S. Cunha, [ID] Rafael Nadas, [ID] Andreij Gadelha, [ID] Luiz Gustavo Cançado [ID] * and Ado Jorio [ID] *

Raman spectroscopy has been established as a valuable tool to study and characterize two-dimensional (2D) systems, but it exhibits two drawbacks: a relatively weak signal response and a limited spatial resolution. Recently, advanced Raman spectroscopy techniques, such as coherent anti-Stokes spectroscopy (CARS), stimulated Raman scattering (SRS) and tip-enhanced Raman spectroscopy (TERS), have been shown to overcome these two limitations. In this article, we review how useful physical information can be retrieved from different 2D materials using these three advanced Raman spectroscopy and imaging techniques, discussing results on graphene, hexagonal boron-nitride, and transition metal di- and mono-chalcogenides, thus providing perspectives for future work in this early-stage field of research, including similar studies on unexplored 2D systems and open questions.

1 Introduction

Raman spectroscopy, the inelastic scattering of light by matter, is established as a powerful tool to image, study and broadly characterize two-dimensional (2D) materials.[1–14] This technique provides important information, such as phononic and electronic properties,[4] number of layers,[15–17] stacking order,[18] phase changes,[19,20] main crystallographic orientations,[1,12,21–24] defect density and type,[5,25] doping,[26–29] functionalization,[30,31] mechanical stress,[29,32] environmental sensing,[33–36] and thermal conductivity,[37,38] among others. Since this technique uses light near the visible spectral range to extract the materials information, it is non-destructive, besides not requiring complex sample preparation processes.[39]

Although Raman spectroscopy is now one the most utilised techniques for 2D materials characterization, it carries two intrinsic limitations: (i) the signal is weak when compared to other light–matter interaction processes, such as elastic scattering and photoluminescence,[40,41] and (ii) the spatial resolution for imaging is limited by diffraction.[42] Regarding the first limitation, the Raman signal is intrinsically weak due to the usually low Raman scattering cross-sections.[40] Therefore, performing Raman spectroscopy can be time-consuming, and the situation is more dramatic in the case of small scattering volumes in low dimensional structures and even worse in Raman imaging, where a large number of Raman spectra are collected at several points when raster-scanning the sample.

Regarding the second limitation, the optical diffraction limit indicates that imaging resolution with light is limited to values close to $\lambda/2$, where λ is the wavelength used for performing the optical imaging. Therefore, in typical Raman spectroscopy measurements the spatial resolution is close to 266 nm for a green laser at 532 nm, considering an ideal optical setup using high numerical aperture objectives. In reality, most typical micro-Raman scattering experiments reach a spatial resolution close to 1 μm[42] due to the use of non-ideal optics.

In this article we review the recent advances in three different Raman-based techniques, which can circumvent the two abovementioned drawbacks related to signal strength and resolution, and their applications in 2D materials, including graphene in Section 2, hexagonal boron-nitride in Section 3, and 2D semiconductors, namely transition metal dichalcogenides (TMDs) and transition metal monochalcogenides (TMMs), in Section 4. We will show how non-linear coherent anti-Stokes Raman spectroscopy (CARS) and stimulated Raman scattering (SRS) can be used to enhance the Raman scattering efficiency in order to perform fast Raman imaging of 2D materials and to learn about light–matter interactions in the non-linear physical regime. We will also show how tip-enhanced Raman spectroscopy (TERS) can be used to extract information with optical resolutions beyond the diffraction limit, therefore accessing new information about 2D materials and about light scattering in the near-field regime. Not only single layer materials ("true" 2D systems) but also many-layer systems, since they are an important part of this research field, will be addressed. We hope that, by organizing this information, we are providing the community with new perspectives for future work that is needed in this early-stage field of research, as discussed in Section 5. However, before

Departamento de Física, Universidade Federal de Minas Gerais, Belo Horizonte, Minas Gerais 30123-970, Brazil. E-mail: lmalard@fisica.ufmg.br, cancado@fisica.ufmg.br, adojorio@fisica.ufmg.br

going into the 2D-materials applications, we first introduce the vibrational structure of 2D materials (Section 1.1) and the basics of the linear and non-linear Raman scattering techniques (Section 1.2) and of the near-field optics overcoming the diffraction limit (Section 1.3).

1.1 Vibrations in 2D materials

Fig. 1 summarizes the structures, vibrational properties and Raman spectra of the different two-dimensional materials discussed in this review. Fig. 1(a, d, g and j) shows the crystal structure with arrows indicating the atomic motions for

certain phonons (named in Fig. 1 according to their symmetry, from group theory[47]) and Fig. 1(b, e, h and k) shows the phonon dispersion relations of the four different categories of 2D materials studied here. From top to bottom: graphene, which is a zero gap semiconductor, hexagonal boron nitride (h-BN), which is an insulator, and materials from the transition metal dichalcogenide family (MoS_2, $MoSe_2$ and WSe_2) and the transition metal monochalcogenide GaS, which are semiconductors.

The Raman spectrum of pristine graphene (Fig. 1(c)) exhibits two features related to different phonon modes with distinct
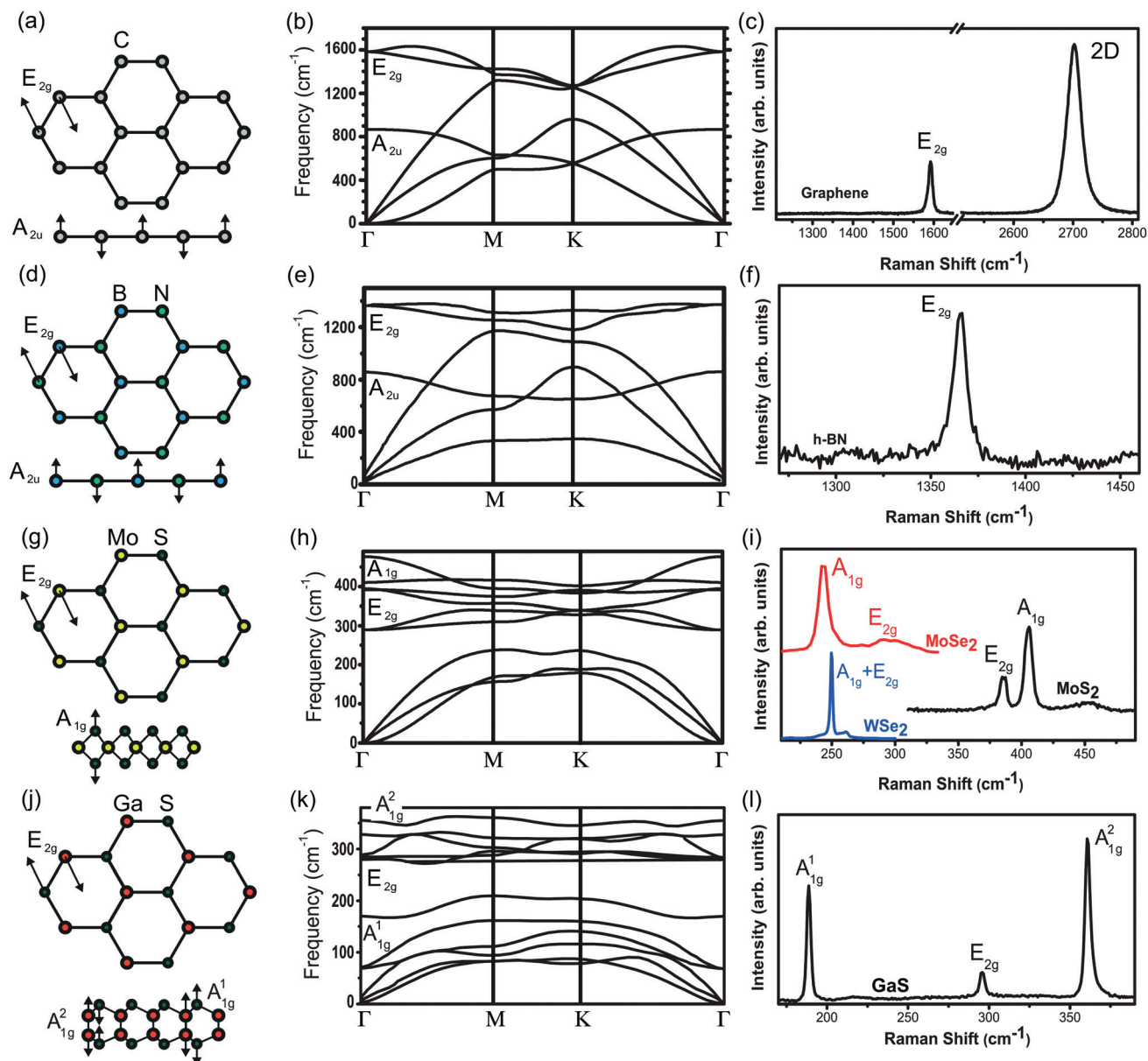

Fig. 1 (a) Top and side (bottom picture) views of the crystal structure of monolayer graphene. (b) Phonon dispersion of graphene showing the high symmetry points and the main phonon modes at the Γ point. Phonon dispersion taken from ref. 43. (c) Raman spectrum of graphene with the main Raman peaks. (d and e) The same as in (a and b) but for monolayer h-BN. Phonon dispersion taken from ref. 44. (f) Raman spectrum of few-layer h-BN. (g and h) The same as in (a and b) but for monolayer MoS_2. Phonon dispersion taken from ref. 45. (i) Raman spectra of monolayer MoS_2, WSe_2 and $MoSe_2$. (j and k) The same as in (a and b) but for GaS. Phonon dispersion taken from ref. 46. (l) Raman spectrum of few-layer GaS. Reproduced with permission from ref. 43–46.

This journal is © the Owner Societies 2021

Phys. Chem. Chem. Phys., 2021, **23**, 23428–23444 | **23429**

symmetries.[4,48] These features are (i) the one-phonon first-order allowed G band (≈ 1580 cm^{-1}), originating from the double-degenerate bond-stretching vibrational mode with E$_{2g}$ symmetry, occurring at the center of the Brillouin zone (Γ point), where the transverse optical (TO) and longitudinal optical (LO) phonon branches touch each other; (ii) the two-phonons 2D band (also called G' in the literature) centered at ≈ 2700 cm^{-1}, originating from the TO phonon branch near the edges (K and K' points) of the graphene Brillouin zone, and generated by double- or triple-resonance processes.[4] Moreover, the 2D Raman band in graphene has been shown to provide important information about stacking order in few-layered graphene.[4,7,15] Notice that the out-of-plane A_{2u} symmetry phonon shown in Fig. 1(a) is infrared active (not Raman active).

For h-BN, Fig. 1(e) shows the phonon dispersion, which is somewhat similar to graphene, where there is an E$_{2g}$ Raman active mode that is doubly degenerate at the Γ point. One important difference is at the K point, where the fact that graphene is composed of a single atom type (carbon), while h-BN is composed of different atoms (B and N) changes the phonon symmetry. A single Raman peak is observed in the Raman spectra of h-BN (see Fig. 1(f)). The presence of two different atoms that break the K-point symmetry also turns h-BN into an insulator (band gap of more than 6 eV), and, consequently, the resonantly enhanced second-order Raman bands typical in graphene or in TMDs are not present for h-BN.

For MoS$_2$ (and others from the TMD family), due to the more complex unit-cell structure, the monolayer phonon dispersion has two Raman-active modes at the Γ point: A$_{1g}$ and E$_{2g}$ symmetries[19] (here we used the bulk nomenclature for the irreducible representations). The corresponding Raman spectrum of MoS$_2$ is shown in Fig. 1(i), where the two most prominent Raman peaks are ascribed to these two first-order modes. Fig. 1(i) also shows the Raman spectra of WSe$_2$ and MoSe$_2$ with the two different first-order Raman peaks. Noteworthily, since these are semiconducting materials, resonance conditions with laser excitation energies close to the exciton states give rise to intense second-order Raman bands, with lineshapes and frequencies depending on the electronic structure and on the resonance condition.[9]

Finally, the bottom line of Fig. 1 shows the structure (j), phonon dispersion (k) and Raman spectrum (l) of a transition metal monochalcogenide, GaS. The structure of the unit cell has more atoms than that of the TMD (4 instead of 3 atoms), and the phonon dispersion has three Raman-active modes at the Γ point: A$_{1g}^2$, E$_{2g}$ and A$_{1g}^1$ symmetries, as shown in the GaS Raman spectrum (Fig. 1(l)).[49]

1.2 Linear and non-linear Raman scattering techniques

Whenever an electromagnetic field interacts with a medium, the electric field $E(t)$ creates a macroscopic polarization $P(t)$. If the amplitude of the polarizing field is small when compared to the intra-atomic fields, the polarization will respond linearly to the applied field, so that[50]

$$P(t) = \varepsilon_0 \chi^{(1)} E(t), \tag{1}$$

where ε_0 is the vacuum electric permittivity and $\chi^{(1)}$ is the linear electric susceptibility of the material. This regime accounts for the usual effects in which the superposition principle holds, such as linear absorption, reflection, refraction and linear Raman scattering (see Fig. 2(a)), the later resulting from phonon-related variations of $\chi^{(1)}$ (for a relation between susceptibility and Raman polarizability, see ref. 4). Fig. 2(a) depicts the energy level description for anti-Stokes (and Stokes) linear and spontaneous Raman scattering, where the scattered photon ω_{as} (ω_s) has a larger (smaller) energy than the incoming photon ω_1 due to its interaction with a vibrational state with energy Ω_ν.

When the amplitude of the electric field becomes sufficiently large as compared to the intra-atomic fields, the optical phenomena do not match the simple linear description of eqn (1). Under this regime, the polarization $P(t)$ can be written perturbatively as a power series:[50]

$$P(t) = \varepsilon_0(\chi^{(1)} E(t) + \chi^{(2)} E^2(t) + \chi^{(3)} E^3(t) + \ldots). \tag{2}$$

The first term in expansion (2) is the same linear polarization regime in (1), while the higher-order terms account for the nonlinear behavior of $P(t)$. Generally, the higher the order n, the smaller the $\chi^{(n)}$ value, and these phenomena were observed mostly after the advent of the laser, where high-enough excitation electric fields $E(t)$ could be achieved. Interestingly, these high-order terms can be engineered to overcome the intrinsic low throughput of the linear (spontaneous) Raman scattering. Actually, different linear and non-linear techniques can be applied with such a goal. Examples of more efficient linear Raman techniques are resonant Raman spectroscopy (RRS), surface-enhanced Raman spectroscopy (SERS) and tip-enhanced Raman spectroscopy (TERS). In RRS, the laser energy is set to be in resonance with absorption bands (usually electronic or excitonic transitions), thus amplifying the Raman scattering probability.[4] SERS uses a substrate with resonant plasmonic nanoparticles in order to enhance the Raman signal of the deposited material.[51–53] TERS is somehow similar to SERS, but the plasmonic nanoparticle is designed as a nanoantenna, which is controlled by a scanning probe microscope, thus enabling imaging by raster-scanning the sample under the nanoantenna.[42] TERS will be introduced in Section 1.3.

The first nonlinear term, driven by $\chi^{(2)}$, is a wave mixing effect known as second harmonic generation (SHG).[50,54] As shown in Fig. 2(b), this three-wave mixing process is characterized by the conversion of two incoming low-energy photons at ω_1 into one photon with exactly twice the incident frequency,[50,54] and it is primarily related to the second term of expansion (2). Due to its coherent and symmetry-sensitive nature,[50,54] in a scanning laser microscope setup with a short-pulsed source, as in Fig. 2(f), SHG enables rapid imaging, providing rich crystallographic information. Such properties make SHG an important technique for the study of many 2D materials.[55–67]

Fig. 2(c) shows a four-wave mixing process, but now related to $\chi^{(3)}$ in the third-order term in expression (2). Three fields are mixed in a nonlinear medium and produce a fourth field,

23430 | *Phys. Chem. Chem. Phys.*, 2021, **23**, 23428–23444
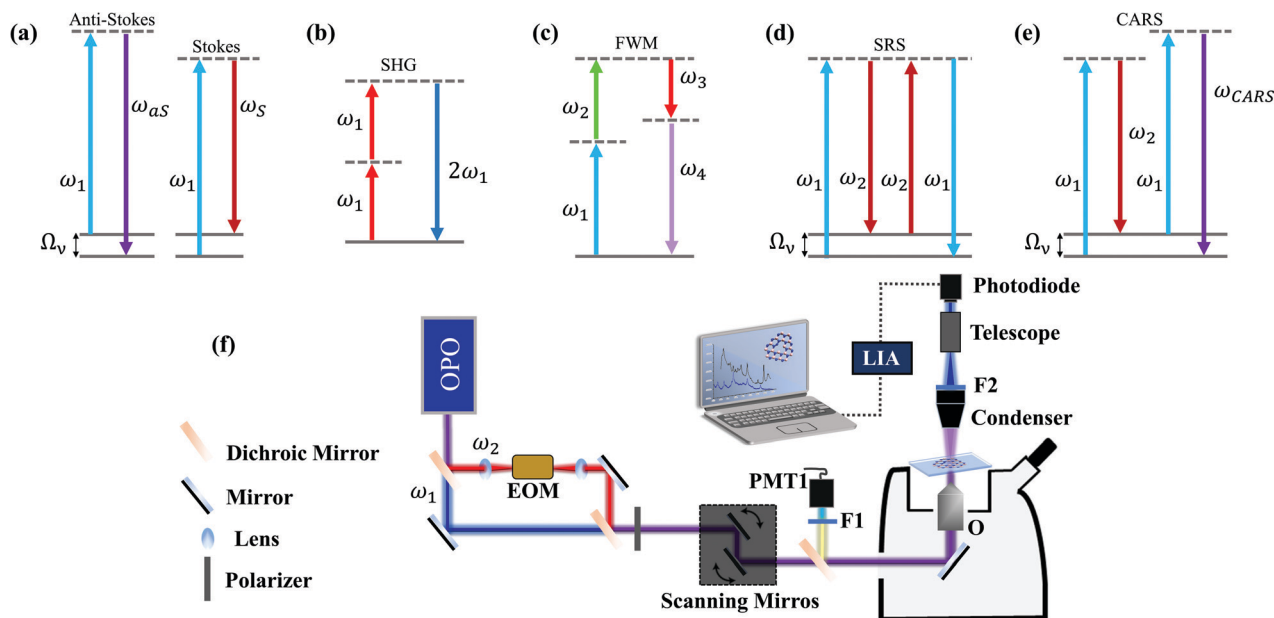
This journal is © the Owner Societies 2021

Fig. 2 Optical linear and nonlinear effects and experimental implementation. Energy level description for (a) anti-Stokes and Stokes linear (spontaneous) Raman scattering, (b) second harmonic generation, (c) general (phonon-unrelated) four-wave mixing (FWM), (d) stimulated Raman scattering (SRS) and (e) coherent anti-Stokes Raman scattering (CARS). (f) Experimental setup for nonlinear imaging. A tunable pulsed laser source (OPO) can provide different excitation wavelengths for imaging and spectroscopy. For general FWM and CARS, the backscattered signal is detected by a photomultiplier (PMT1) with a suitable band-pass filter (F1). The forward SRS is detected by a large-area photodiode with a filter (F2) blocking the beam initially modulated by the electro-optic modulator (EOM, not needed for CARS). The initially unmodulated beam is detected through a modulation transfer scheme mediated by a lock-in amplifier (LIA).

characterizing the process of traditional four-wave mixing (FWM).[50,54] There are several possible energetic configurations for the FWM process in Fig. 2(c), for different choices of ω_i, and our focus here is on the nonlinear Raman spectroscopies, namely coherent anti-Stokes Raman spectroscopy (CARS) and stimulated Raman scattering (SRS), which are techniques where the Raman cross-section is enhanced significantly by optically stimulating phonons in the materials in the third-order process in eqn (2).

When two fields at frequencies ω_1 and ω_2 interact coherently in a nonlinear medium, Raman-mediated effects arise when the beating frequency ($\omega_1 - \omega_2$, with $\omega_1 > \omega_2$) is resonant with a vibrational transition at Ω_v.[41] Fig. 2(d) shows the conversion of ω_1 into ω_2, stimulated by the presence of the beam at ω_2 at the cost of leaving the material in an excited vibrational state. Such a process is stimulated Raman scattering (SRS).[41,50,54] Simultaneously, the beam at ω_2 also stimulates a FWM process that generates the ω_{CARS} frequency at $2\omega_1 - \omega_2$, which characterizes the coherent anti-Stokes Raman scattering (CARS)[41,50,54] in the diagram in Fig. 2(e). In both cases, the stimulated generation of ω_2 and ω_{CARS} (in SRS and CARS, respectively) is orders of magnitude more likely to occur than in the spontaneous Raman scattering in Fig. 2(a).[41,68] As a Raman-mediated four-wave mixing, SRS and CARS probe vibrational states, therefore providing also chemical fingerprints of the materials. The fundamental difference between CARS and SRS is that the first is a parametric effect, while the second is a dissipative effect. In CARS, the interaction between the fields takes place without

changing the final state of the material, i.e. the full process is coherent. Experimentally the CARS signal is measured by a photomultiplier with an appropriate band pass filter at the anti-Stokes Raman frequency, as shown in Fig. 2(f). On the other hand, the SRS occurs only when there is an energy transfer, leaving the material in an excited vibrational state.[41] This ensures no interference between SRS and non-resonant FWM processes, which gives the technique a better signal-to-noise ratio. Experimentally, for measuring SRS the laser at the Stokes frequency is intensity-modulated and the pump laser intensity is measured by a photodiode at the same modulation frequency, by using a lock-in amplifier after the sample, as shown in Fig. 2(f). Combined with the stimulated nature of the process, SRS allows Raman-specific and high-speed imaging with excellent contrast, which can be used to study 2D materials.

The applications of CARS and SRS will be discussed in Section 2.1 for graphene, Section 3 for h-BN and Section 4.1 for TMD semiconductors.

1.3 Overcoming the diffraction limit using TERS

The idea of using the near-field to overcome the limitation of spatial resolution imposed by light diffraction in optics was proposed in 1928.[69] However, the experimental implementation of this idea in the visible spectral range had to wait for the development of scanning probe techniques,[70–72] since in this frequency range the near-field is lost in a few nanometers away from the emitter. Although different technological approaches have been utilized to implement this technique, as described
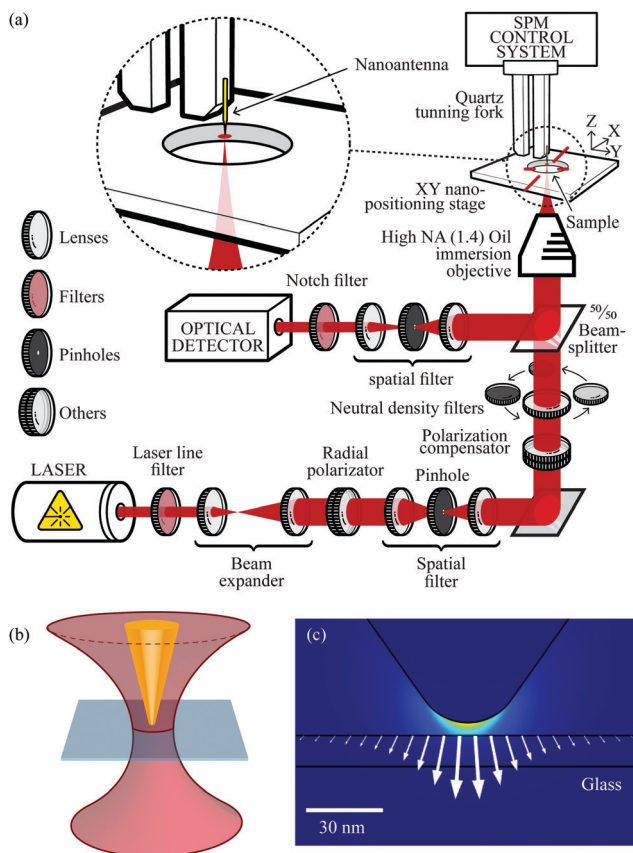
This journal is © the Owner Societies 2021

Phys. Chem. Chem. Phys., 2021, **23**, 23428–23444 | **23431**

Fig. 3 (a) Schematics of a tip-enhanced nano-optics system. The sample is located in the *XY* positioning stage, where the excitation field, coming for a laser, reaches the sample and the nano-antenna. This exemplary system works in a back-scattering configuration, with the optical system at the bottom and the scanning probe system at the top.[83] (b) Schematics of the excitation field focus (reddish), where the nano-antenna (tip, yellowish) has to be positioned,[84] near the sample on the transparent substrate (grayish). (c) Field intensity simulation (bright colors indicate high fields) near the tip apex. The arrows indicate the field vectors at the sample surface.[85] Reproduced with permission from ref. 83 and 85.

extensively in the literature (see ref. 42 and references therein), here we focus on the most promising solution for addressing 2D systems, which is tip-enhanced Raman spectroscopy (TERS;[73–80] we will also address tip-enhanced photoluminescence – TEPL[70,81,82]).

The technical aspects behind a tip-enhanced system are shown in Fig. 3, in which panel (a) illustrates the combination of an optical spectroscopy system with a scanning probe microscope driving the optical tip or nanoantenna. The optical system is composed of devices for excitation and back-scattered detection of the optical spectra, including a laser, a spectrometer and a diversity of optical devices to condition the laser beam, which has to be properly coupled to the nanoantenna.[83] Fig. 3(b) illustrates the region wherein the far-field emission from the objective is focused at the nanoantenna (tip).[84] Fig. 3(c) shows a simulation of the local field near the tip apex, thus generating the local (near-field) tip-enhanced field.[85] The sample is located a few nanometers below the tip and

raster-scanned, thus generating hyperspectral data that can be used to generate 2D images.

Tip-enhancing strategies are especially challenging when addressing 2D materials[80,86] because the illumination of the nano-antenna is performed with a propagating field, which therefore illuminates the sample over a much larger area (micrometric dimensions) as compared to the locally antenna-enhanced field (nanometric in size). This competition is not relevant when addressing zero-dimensional (0D) structures, for instance, a molecule or a single defect in a 2D crystal lattice, or even a one-dimensional emitter, such as a carbon nanotube or the edge of a 2D material. However, to address local changes in the intrinsic properties of 2D systems, the nano-antenna enhancement has to be enough to overcome the signal coming from an area roughly 10^3–10^4 times larger. Such enhancements are obtainable in surface-enhanced Raman scattering (SERS) because ultra-high fields are generated in the hot-spots, the gap between plasmonic-resonant nanoparticles (gap-mode configuration). The same is not true, however, for TERS in a non-gap mode configuration. For this reason, substantial efforts have been devoted in the TERS community to develop efficient nano-antennas.[82,87–89] The recently developed plasmon-tuned tip pyramid (PTTP) is especially interesting,[90–92] which enabled two-orders of magnitude spectral enhancements[91,92] and the observation of crystallographic Moiré structures in low-angle twisted bilayer graphene (TBG).[93]

The science of 2D systems based on TERS (and some TEPL) will be discussed in Section 2.2 for single-layer graphene, Section 2.3 for low-angle twisted-bilayer graphene and Section 4.2 for layered semiconductors in the family of transition metal (di)(mono)chalcogenides.

2 Graphene

2.1 CARS

Four-wave mixing studies in graphene were done by Hendry *et al.* in 2010, where the authors obtained a large value of the third-order electrical susceptibility of graphene.[97] Other authors have characterized the $\chi^{(3)}$ of graphene by different techniques, such as third-harmonic generation, and also reported large susceptibility values, opening up different possible applications.[67] However, none of these studies utilized laser energies that are close to resonance with phonon energies, which is the condition for CARS (see Section 1.2). When the FWM is in the CARS condition, it is expected that the anti-Stokes signal will be enhanced due to the resonance with the phonons, *i.e.* $\omega_1 - \omega_2 = \Omega_\nu$. Unexpectedly, Lafeta *et al.* showed that, in the case of graphene, the FWM signal intensity decreases when in resonance with the phonon energy.[94] This phenomenon occurs in graphene because it is a zero-gap semiconductor with a strong contribution of electronic transitions to the third-order nonlinear electrical susceptibility,[94] and not only due to transitions involving the phonon state, as depicted in Fig. 4(a). In order to understand this effect in more detail, it is convenient to separate the third-order polarization in two parts: a
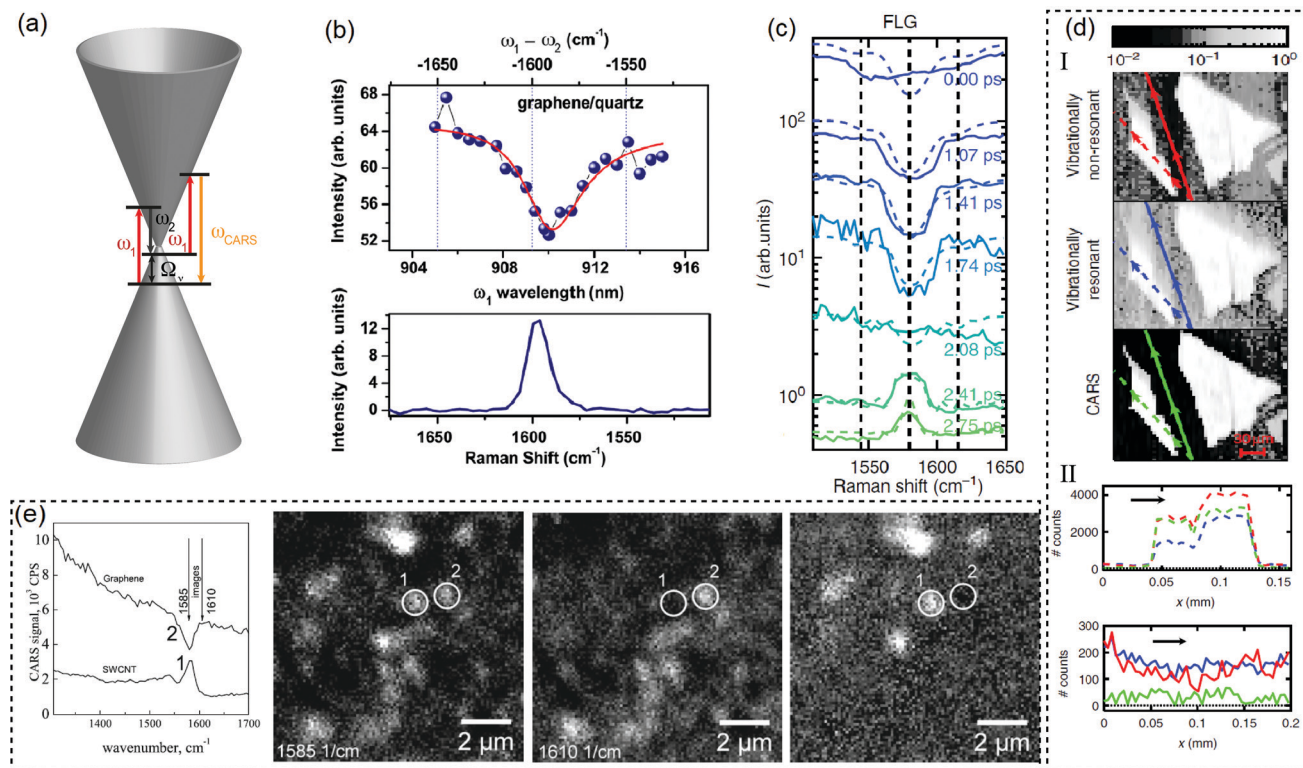
23432 | *Phys. Chem. Chem. Phys.*, 2021, **23**, 23428–23444

This journal is © the Owner Societies 2021

Fig. 4 (a) Band structure of graphene (cones) and the CARS process (arrows) where two laser frequencies ω_1 and ω_2 interact with the material generating an anti-Stokes signal at $\omega_4 = \omega_{CARS}$ frequency. (b) Top: CARS (ω_4) intensity as a function of the ω_1 pump wavelength (bottom scale) or $\hbar\omega_2 - \hbar\omega_1$ in wavenumbers (top scale) for graphene on a quartz substrate. The bottom graph shows the Raman spectrum taken in the same energy range.[94] (c) CARS spectra of few-layer graphene at different delay times between the ω_1 and ω_2 laser pulses. (d) I: CARS images of two few-layer graphene flakes; from top to bottom: outside vibrational resonance, under vibrational resonance, and by posterior calculations. II: intensity line profiles along the sample (dashed lines in I) and substrate (full lines in I).[95] (e) The graph on the left side shows the SWCNT (1) and graphene (2) CARS spectra. The leftmost image shows a CARS image of the SWCNT/graphene system obtained at 1585 cm^{-1} at resonance with the phonon. The next image is the same sample region but taken at 1610 cm^{-1}, outside the phonon resonance. The rightmost image is the difference between the previous images obtained at 1585 cm^{-1} and 1610 cm^{-1}. Points no. 1 and no. 2 represent the SWCNT and graphene locations, respectively.[96] Reproduced with permission from ref. 94–96.

nonvibrationally resonant background (NVRB) polarization ($P_{NVRB}^{(3)}$) and a vibrationally resonant background (which we call CARS, for convenience) polarization ($P_{CARS}^{(3)}$).[95,98] Because the intensity measured at the anti-Stokes frequency is given by $I(\omega_{as}) \propto |P_{CARS}^{(3)} + P_{NVRB}^{(3)}|^2$, there is an interference between the two terms that can lead to a decreased intensity at the anti-Stokes frequency, when $\omega_1 - \omega_2 = \Omega_\nu$.[94,95] Fig. 4(b) shows the FWM spectrum of graphene taken at different values of pump laser energy (ω_1), where it is possible to observe that the intensity decreases exactly at the G-band phonon energy, as confirmed by linear Raman spectroscopy (see the bottom graph of Fig. 4(b)).[94]

Moreover, Virga *et al.* showed that the temporal evolutions of $P_{NVRB}^{(3)}$ and $P_{CARS}^{(3)}$ are significantly different, where in the case of NVRB the FWM interactions must take place within the dephasing time of the involved electronic transitions, which is close to 10 fs for graphene.[95] On the other hand, the phonon dephasing time in graphene is much longer (1 ps), and hence while $P_{NVRB}^{(3)}$ has a fast dephasing time, $P_{CARS}^{(3)}$ has a much longer dephasing time. This effect is shown in Fig. 4(c) where the anti-Stokes intensity is measured for different delay times between the two laser pulses. At zero delay time, the CARS spectra shows

a decreased intensity at the phonon energy. However, when the delay time is increased, the CARS intensity slowly increases and reaches a maximum at longer delay times, corresponding to the $P_{CARS}^{(3)}$ term.[95]

For performing CARS imaging in graphene, one needs to take into account the strong contribution of the FWM signal from electronic transitions. Virga *et al.*[95] accomplished this by measuring a set of images as shown in Fig. 4(d) in panel I. In the first image (from top to bottom) the authors have measured the CARS intensity of few-layer graphene at a frequency away from the phonon resonance, with a strong contribution from $P_{NVRB}^{(3)}$. In the second image, they have displayed the CARS intensity at the phonon resonance where both $P_{NVRB}^{(3)}$ and $P_{CARS}^{(3)}$ have contributions. In the third image, the authors have performed a calculation based on the first two images to obtain a high contrast CARS image.[95] Fig. 4(d) in panel II shows an intensity profile along the graphene flake (top graph with dashed lines) and at the substrate (bottom graph with full lines). It is possible to observe that the procedure for producing the CARS image shown in panel I have a small intensity coming from the substrate and a high intensity coming from the graphene flake, therefore enabling high contrast CARS imaging in graphene.[95]

This journal is © the Owner Societies 2021

Phys. Chem. Chem. Phys., 2021, **23**, 23428–23444 | **23433**

Fig. 4(e) shows another example of CARS imaging in graphene together with single-walled carbon nanotubes (SWCNT)[99] using a similar methodology.[96] The first graph (on the left) shows the CARS spectra of both graphene and SWCNT near the G band frequency, where it is possible to observe the decreased intensity of CARS near the phonon energy for graphene (spectrum 2), but an enhanced intensity for SWCNT (spectrum 1). In the first CARS image taken in resonance with the phonon energy, both SWCNT and graphene are located in the highlighted regions 1 and 2, respectively. On the other hand, away from the phonon resonance (second CARS image) the SWCNT signal disappears, while the graphene signal remains due to the signal coming from the non-resonant contributions, as discussed before. Finally, in the last CARS image the authors performed a subtraction between the first two images, showing that the signal coming from the SWCNT is enhanced in the image compared to the signal coming from graphene.[96]

2.2 TERS in graphene

One-dimensional (1D) carbon nanotubes were initially explored as an important prototype for the development of tip-enhanced Raman spectroscopy (TERS),[75,102–105] mostly due to their strong resonant Raman scattering associated with their 1D structure. Later on, 2D graphene became a protagonist of the development of fundamentals and applications of TERS, for reasons we explore here.

TERS has been utilized to identify local strain and doping in in-plane homojunctions in graphene devices, built as van der Waals heterostructures where the graphene is half sitting on talc and half on SiO_2.[106] The high spatial resolution of TERS enables the observation of the charge depletion region at the interface between different substrates. Furthermore, local strain and doping can also result simply due to the presence of particles in the substrate[107] or due to non-homogeneous deposition when forming twisted bilayer graphene.[108] Such non-homogeneity is only identifiable with nano-Raman, while it is averaged out in usual micro-Raman analysis.[108]

More than just improving imaging spatial resolution, the different symmetries and dimensionalities of the features composing the Raman spectrum of graphene provide a fertile source of new phenomena occurring in the near-field regime and reveal the important aspects of TERS.[109,110] The most fundamental one is the influence of interference effects on the TERS signal.[100,111] Spatial correlations of phonon modes can be neglected in conventional Raman spectroscopy experiments performed in the far-field regime because the correlation length L_c of optical phonons in crystals is one order of magnitude shorter than the wavelength of visible light.[111,112] According to the early theory of coherence, optical fields present correlation lengths of at least half of their associated wavelength in the far-field regime.[113] Therefore, the information on shorter correlations of the source is lost when the signal transits to the far zone (more than half wavelength far from the source). For this reason, Raman scattering is usually treated as a spatially incoherent process in classical textbooks,[114] which do not account for the near-field components of the scattered field. However, with the advent of TERS, it has been shown that this approach is not valid when the non-radiating near-field components are taken into account.[86,100,110,111,115] Due to coherence, the Raman intensity at the nanoscale depends on the symmetry and spatial confinement of the vibrational mode. The characteristic length that defines this spatial correlation can be extracted from the different levels of enhancement measured for distinct modes. In short, the interference is destructive for the G band signal, associated with phonons with E_{2g} symmetry, and constructive for the D and 2D bands, associated mostly with totally symmetric A_{1g} phonons[110] (see Fig. 5(a)). As such, the interference effects give rise to a weaker tip–sample distance dependence for the G band than for the D and 2D bands, making it possible to extract the correlation length $L_c \sim 30$ nm from the measured data.[100,111] Moreover, if the D band signal originates from edges (1D structure), a further change of the tip–sample distance dependence is observed. The experimental evidence for these coherence phenomena was first reported in ref. 111. Later on, similar effects were reported for GaS[116] (see Section 4.2).

Besides the correlation length of optical phonons, the distinct behavior of the 2D and G bands in the near-field regime can be used as a measurement for the enhancement achieved in a TERS experiment. This effect is summarized in Fig. 5(b), reproduced from ref. 101. The solid circles are the experimental data extracted from the ratio of the integrated areas of the 2D and G bands (A_{2D} and A_G, respectively), measured from a pristine graphene sample as the near-field probe (a plasmon-tunable tip pyramid – PTTP)[90–92] approaches the surface by shortening the tip–sample distance Z. The values are normalized to the far-field signal so that $A_{2D,D}/A_G \rightarrow 1$ for larger values of Z. As shown in the graphics, for the minimal distance at $Z \rightarrow 0$ (which means the tip is roughly 5 nm away from the sample), the enhancement of the 2D band is approximately twice the enhancement exhibited by the G band, with the difference decreasing as Z increases. The blue solid line is a fitting of A_{2D}/A_G as a function of Z according to the theory developed in ref. 100. The fit indicates a field-enhancement factor f of approximately 4.5. This enhancement factor is related to the tip polarizability, and it is a measure of its strength for local field enhancement. The orange dotted and green dashed curves are plots of theoretical calculations considering hypothetical experiments with tips that would provide field-enhancement factors of 2 and 6, respectively.

In the presence of structural defects that break the translational symmetry of the graphene lattice, the Raman spectrum is also composed of the disorder-induced D band (≈ 1350 cm^{-1}), originating from the same TO phonon branch that gives rise to the 2D band, and also by the D′ band (≈ 1620 cm^{-1}), originating from the LO phonon branch in the proximity of the Γ point [see the bottom spectrum in Fig. 5(a)].[4] Because D and D′ require structural defects to satisfy momentum conservation in the double-resonance Raman process, their sources are localized in the defective region, and therefore they have the same dimensionality as the defect itself.[117,118] In other words, point and edge defects give rise to D or D′ bands originating from zero- and one-dimensional regions, respectively.[25]
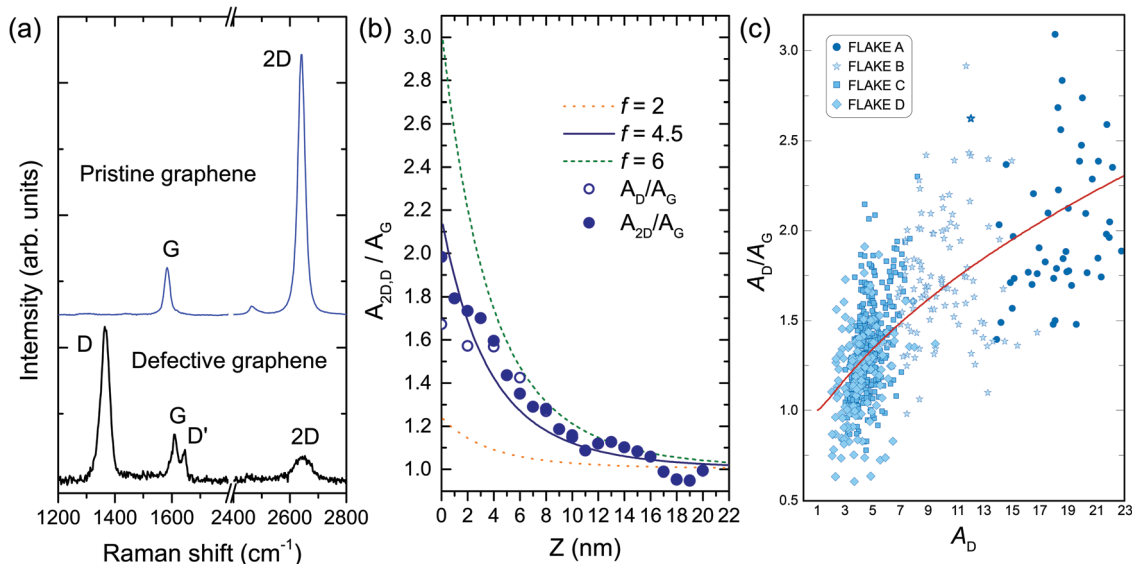
Fig. 5 (a) At the top, the Raman spectrum of pristine graphene composed of the one-phonon first-order allowed G band (≈ 1580 cm^{-1}) and the two-phonon 2D band (also called G′ in the literature) centered at ≈ 2700 cm^{-1}. In the presence of structural defects that break the translational symmetry of the graphene lattice, the Raman spectrum is also composed of the disorder-induced D and D′ bands, centered at ≈ 1350 and 1620 cm^{-1}, respectively, as shown in the bottom spectrum. (b) Solid circles: experimental data extracted from the ratio of the integrated areas of the 2D and G bands (A_{2D} and A_G, respectively), measured from a pristine graphene sample as the near-field probe (a plasmon-tunable tip pyramid – PTTP)[90–92] approaches the surface by shortening the tip–sample distance Z. Open circles: A_D/A_G data from the tip-approach procedure conducted in a defective graphene nanoflake. Solid blue line: fitting of A_{2D}/A_G as a function of Z according to the theory developed in ref. 100. The fit indicates a field-enhancement factor f of approximately 4.5. Orange dotted and green dashed curves: plots of theoretical calculations considering hypothetical experiments with PTTPs that provide field-enhancement factors of 2 and 6, respectively. (c) Scatter plot of A_D/A_G values as a function of A_D for four distinct nanoflakes (marked by distinct symbols) investigated in ref. 101. The red solid line is the result of a theoretical fit of the data points using a relation developed in ref. 101 based on the theoretical background introduced in ref. 100. From left to right, the red line defines a trajectory for larger values of the enhancement factor f giving rise to larger values of A_D/A_G. The values of A_D, A_G and A_{2D} in (b) and (c) are normalized to their respective far-field values. Reproduced with permission from ref. 101.

The graphics also exhibit the A_D/A_G data (open circles) from the tip-approach procedure conducted in a defective graphene nanoflake. As explained above, since the D and 2D bands have the same symmetry, they are indeed expected to exhibit the same near-field interference properties. Therefore, the dependence of the A_D/A_G ratio on the field enhancement factor has important metrological consequences in terms of determination of defect density in graphene by TERS.[101] It is well known that the A_D/A_G ratio is sensitive to the amount of structural defects.[9,25,29,112,117] In the absence of sp³ bonds, the A_D/A_G ratio is inversely proportional to the squared average distance between point defects L_D[2,25,117,119] or to the average crystallite size, L_a, in the case of linear defects.[25,112,120] For conventional Raman spectroscopy, these relations were established through the measurement of prototype samples with L_D and L_a previously determined by scanning tunneling microscopy (STM).[112,117,120] However, because the enhancement factor influences the value of the A_D/A_G ratio, as demonstrated in ref. 101 and 111 (see Fig. 5(c) and related text), metrological protocols that take into account the enhancement factor of the near-field probe used in the experiment have to be developed[101] for quantitative analysis with TERS. This is an open field for TERS application.

2.3 TERS on twisted bilayer graphene

The ability to precisely tune the angle between two layers of graphene opens the possibility for an extra degree of

nanomanipulation that led to the discovery of unconventional superconductivity in twisted bilayer graphene (TBG) at the so-called magic angle (twist angle $\theta \sim 1.1°$).[121,122]

In real space, twisted homo-bilayer heterostructures form an artificial lattice, frequently called moiré patterns, whose lattice constant (L_m) is angle-dependent following the equation: $L_m = a_0 \left/ \sqrt{\frac{1}{2}\sin(\theta/2)} \right.$, where a_0 is the single-layer lattice constant. $L_m \geq 10$ nm for angles $\theta \leq 1°$ in twisted bilayers from graphene, hexagonal boron nitride (h-BN) and TMDs. Recently, Yoo et al. showed that, for $\theta \leq 1°$, the TBG experiences an energetically favorable atomic reconstruction, generating the so-called reconstructed twisted bilayer graphene (rTBG),[123] where the carbon atoms rearrange to maximize the AB and BA stacking regions, alternating black and gray triangles, as shown in Fig. 6(a). The AB and BA stacking are similar but differ by a reflection operation. Moreover, saddle point (SP) solitons (frequently called just solitons) separate the AB/BA domains. Finally, the interception between the SP solitons forms topological AA stacked points (Fig. 6(a)). Notably, TMDs also show reconstruction below a critical angle.[124] Here, we focus on near-field imaging of rTBG because of its particular arrangement with well-defined regions.

So far, most near-field studies in rTBG used infrared (IR) excitation (with excitation energies ranging from 100 to 200 meV).[125–127] Nano-IR successfully investigated plasmonic,
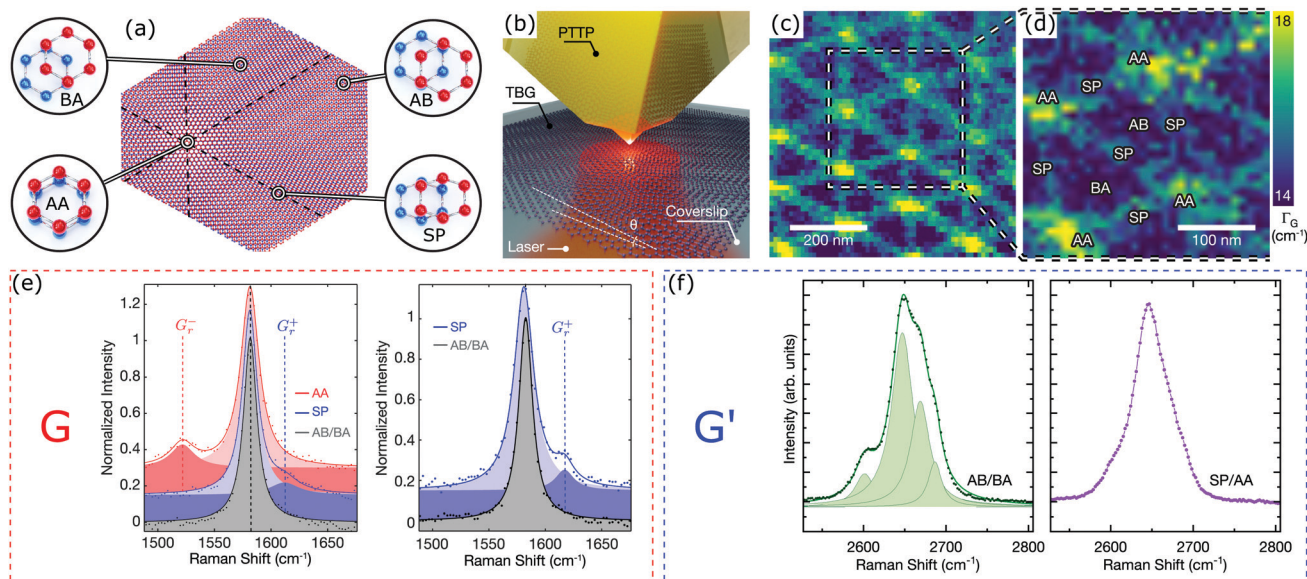
This journal is © the Owner Societies 2021

Phys. Chem. Chem. Phys., 2021, **23**, 23428–23444 | **23435**

Fig. 6 (a) Representation of rTBG. (b) Sketch of rTBG imaging by nano-Raman highlighting the TERS tip (PTTP – plasmon–tuned-tip pyramid). (c) Nano-Raman rTBG map recorded from the G′ (also named 2D) band intensity. (d) G-band FWHM nano-Raman map acquired at the dashed square in (c). (e) Nano-Raman G-band spectra recorded in AA (red), SP (blue) and AB/BA regions. The left panel data were acquired in the same sample as in (d), and the right panel data were from another location with a single soliton. (f) Nano-Raman G′ spectra from the AB/BA (left) and SP/AA (right) regions. Reproduced with permission from ref. 93.

electronic and thermoelectric rTBG solitonic properties, but this technique has two significant limitations that prevent a complete investigation over rTBG quantum properties: (1) most of the in-plane rTBG phonons are IR dipole-forbidden;[128] (2) the tips for nano-IR generate a relatively low near-field signal.[125–127] In contrast, TERS-based nano-Raman spectroscopy gives a multi-assessing tool, allowing phonon, electron, electron–phonon coupling and stacking-order investigations in rTBG. The TERS nanoantenna (see Fig. 6(b)) induces localized near-field signals orders of magnitude larger than the far-field signals, providing a pure near-field contribution restricted to the tip apex location. Fig. 6(c) presents a nano-Raman map recorded from the rTBG G′ (also named 2D) band intensity.[93] The map unravels an L_{m} = 160 nm (θ = 0.09°) rTBG crystallographic structure, where the AB/BA, SP, and AA stacking regions are observed. Note that nano-Raman does not distinguish AB/BA because their Raman selection rules are the same.

Besides revealing the crystallographic structure of rTBG using visible light, nano-Raman carries rich physical information. Close to the Fermi level, the low-energy G phonons ($E_{\mathrm{ph}} \approx$ 197 meV) mediate electronic transitions, enhancing the electron–phonon coupling (EPC). As the EPC increases, the G phonon lifetime decreases and enlarges the full-width at half maximum (FWHM),[26,28] *i.e.* the G band FWHM indirectly probes the EPC. Fig. 6(d) presents the image of the G band FWHM over the dashed square in Fig. 6(c). The FWHM outlines the rTBG crystallography where higher values of FWHM (*i.e.* higher EPC) are observed at the AA sites due probably to density of states localization.[129,130] Nevertheless, Xie *et al.* also showed that a strong electron–electron interaction is expected at the AA points[131] and similarly for the EPC in Fig. 6(d).

So Fig. 6(d) indicates the possibility that the EPC plays a role in TBG superconductivity.

Fig. 6(e) presents the nano-Raman G spectra acquired in the AA (red), SP (blue), and AB/BA (black) regions. The data from the left panel were acquired from the sample in Fig. 6(d), while the right panel displays data from another location near a single soliton. All the spectra exhibit a pronounced G band, but at the SP and AA locations they also present higher and lower frequency peaks, named G_{r}^{+} and G_{r}^{-}, respectively. Gadelha *et al.* revealed that the G_{r}^{+} mode is mostly observed at the SP, while the G_{r}^{-} at the AA.[93] A state-of-the-art nearly free phonon model also supports the results.[129]

On the other hand, the electronic structure, stacking order, and other factors impact the G′ mode. Fig. 6(f) presents the nano-Raman G′ spectra acquired in the AB/BA (left panel) and SP/AA (right panel) regions. The AB/BA nano-spectrum is identical to that of Bernal-stacked bilayer graphene, composed of four peaks (see Fig. 6(f)), as expected.[15] However, the SP/AA spectrum exhibits an unusual lineshape, providing a unique Raman signature. Therefore, Fig. 6(e and f) manifest a localization of both the phononic and electronic rTBG aspects.[129,130]

3 Hexagonal boron nitride – CARS and SRS

Similar to the case of graphene (see 2.1), Lafeta *et al.* studied the FWM response of h-BN close to the CARS condition. The band structure of h-BN is schematically shown in Fig. 7(a), where it is indicated that h-BN is an insulator with a high value of band gap. Therefore, the CARS process in h-BN does not have
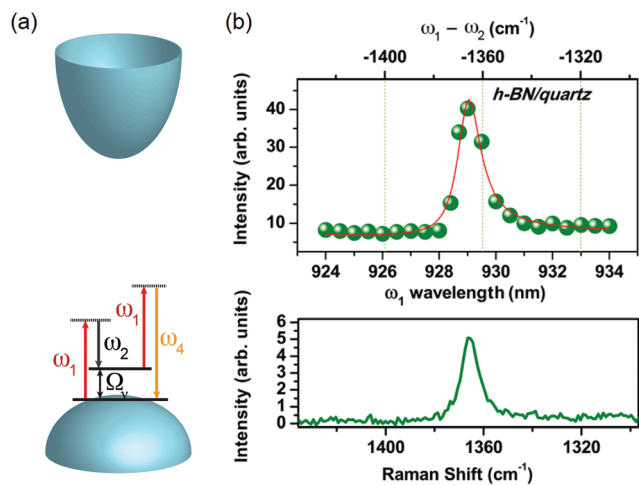
Fig. 7 (a) Schematics of the band structure of h-BN (paraboloids), which is an insulator, with the diagram of the CARS process (arrows), where two lasers of frequencies ω_1 and ω_2 interact with the material generating an anti-Stokes signal at the ω_4 frequency. (b) CARS spectra of few-layer h-BN as a function of the ω_1 wavelength (bottom scale) and $\hbar\omega_2 - \hbar\omega_1$ in wavenumbers (top scale) for few-layer h-BN. The Raman spectrum of the same sample is shown in the graph below. Reproduced with permission from ref. 94.
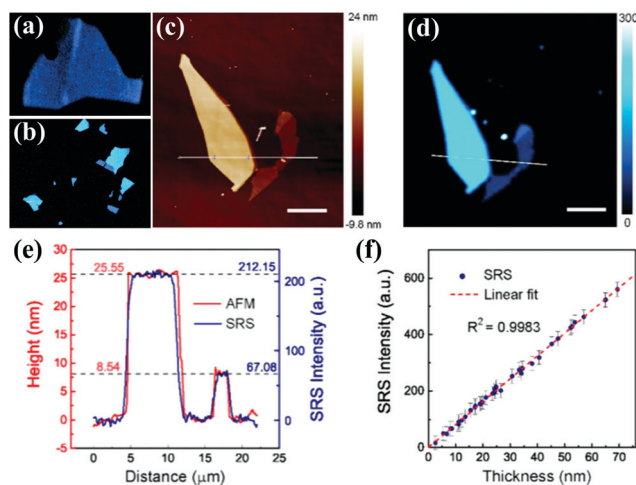

Fig. 8 (a) SRS image of an h-BN flake and (b) a large-area image of a different area of the sample obtained with a high numerical aperture objective in a setup similar to the one in Fig. 2(e). (c) AFM and (d) SRS images of an h-BN sample. (e) AFM heights and SRS intensities along the lines shown in (c and d). (f) Dependence of SRS intensity on flake thickness. Reproduced with permission from ref. 136.

a contribution from the electronic NVRB, and the CARS spectra will have only contributions from the phonon resonance. The CARS spectra of h-BN are shown in Fig. 7(b), where it is possible to observe an enhancement when both lasers have an energy difference matching the phonon energy, which is corroborated by the Raman spectra shown in the bottom graph.[94]

As discussed in Section 1.2, the stimulated and dissipative nature of SRS allows the study of materials by rapid imaging and spectroscopy. In the case of h-BN, this is of particular importance. As a wide bandgap material, it can be difficult to study its properties using absorption-based optical contrast techniques. In addition, its E_{2g} Raman-active mode is far from electronic resonances, giving h-BN a weak Raman signal when compared to other 2D materials. The E_{2g} mode is about 50 times stronger in graphene.[132] While this limits the research of h-BN through spontaneous Raman scattering, this also illustrates one of the main advantages of SRS. Fig. 8(a) and (b) show high-resolution images of a mechanically exfoliated h-BN flake and a large area image with several flakes, respectively, both obtained by SRS with a total acquisition time of less than one minute.

Although SRS is widely used in bioimaging,[41,133–135] it has only recently been applied to study 2D materials and, in particular, h-BN.[136] While spontaneous Raman scattering has been used to characterize the number of layers of few-layer h-BN, some authors[44,136] call attention to discrepancies between some results and extensions for multilayers.[132,137–140] Using SRS, Ling et al.[136] addressed this controversy, measuring 35 mechanically exfoliated flakes with thickness ranging from 2.5 nm to 70 nm. Fig. 8(c) and (d) show, respectively, the AFM and SRS images of an h-BN flake. We can immediately observe a close correspondence, suggesting a relation between the thickness of the material and the SRS intensity. A line profile

across the regions of different thicknesses (see locations in Fig. 8(c) and (d)) allows the comparison of the intensity profiles from AFM and SRS, which shows the very well-matched curves in Fig. 8(e). From the intensity profiles of AFM and SRS, Ling et al. obtained the linear dependence of SRS intensity on sample thickness, as shown in Fig. 8(f). This result suggests the possibility of using SRS to quantify sample thickness in a rapid manner. It is worth mentioning that, regarding Raman spectroscopy in non-transparent media, the penetration depth depends on the laser wavelength and the material index of refraction, ranging from a few nanometers to hundreds of microns. In the case of h-BN, which is transparent at the laser energies typically used for SRS, the material thickness can be probed. Moreover, the authors acquired the SRS images with a pixel dwell time that is 4 orders of magnitude smaller compared to conventional spontaneous Raman microscopy, highlighting the promising use of the technique in the research of h-BN.

4 2D semiconductors

4.1 CARS

CARS has not yet been widely applied to the study and imaging of 2D semiconductors, such as TMDs, mainly because of their low vibrational frequencies as compared to other 2D materials, such as graphene and h-BN. In commonly available laser systems, there are experimental difficulties in matching the pump and Stokes laser energies with the low vibrational frequencies in these materials. Nevertheless, multiplex CARS spectroscopy was used by Ko et al. to investigate processes in bulk MoS_2.[141] The authors have used a photonic supercontinuum fiber to generate a broad band Stokes pulse ranging from 800 to 1100 nm and a narrow band pump pulse centered at

This journal is © the Owner Societies 2021

Phys. Chem. Chem. Phys., 2021, 23, 23428–23444 | 23437

800 nm. The measured CARS spectra were characterized by a broad peak corresponding to the four-wave mixing signal of MoS_2 and another peak centered at approximately 680 nm, corresponding to a resonance with the A exciton. Moreover, the authors identified a smaller peak in the CARS spectra that corresponds to a vibrational energy of 634 cm^{-1}, which corresponds to a combination between A_{1g} and LA(M) phonons.[141] Further progress needs to be made in order to overcome the experimental limitations for performing CARS in TMDs and other 2D materials with low frequency Raman modes.

4.2 TERS

After graphene, the TMD MoS_2 (see Fig. 1(g)) is the most studied 2D material using TERS. The first report of tip-enhanced measurements in MoS_2 shows a nanoscale mapping of excitons and trions by combining TERS and TEPL, with a spatial resolution of less than 20 nm.[146] The authors also investigated doping by using Ag and Au coated tips and found that the type of doping depends on the work function of the metal, n-doping for Ag and p-doping for Au. Thus, using an Ag coated tip, it was possible to create a TEPL mapping of the A^0 exciton and for the A^- and B^- trions in single-layer MoS_2. Following this work, other authors contributed to the development of this field. For instance, a giant gap-mode TERS was performed in MoS_2 with the aid of a nanocluster array on the substrate.[142] As shown in Fig. 9(a), a 10^8 enhancement was observed for the A_{1g} peak. Notice the A_{1g} was enhanced much more than the E_{2g}, consistent with the near-field coherence effect discussed for graphene (Section 2.2).[100,111] This large

enhancement is attributed to the presence of nanodisks of gold on the substrate (displayed on the right side of Fig. 9(a)), creating the gap-mode regime that provides high enhancement on the edges of the disks. The authors also observed a plasmonic hot electron doping of monolayer MoS_2 due to the presence of the tip and the nanodisks on the substrate, which caused a transient structural phase transition from 2H to 1T.[19]

TERS has also been used to study highly localized strain in MoS_2/Au heterostructures induced during the formation of such a heterostructure, in which the maximum shift reported for the E_{2g} mode was (4.2 ± 0.8) cm^{-1}, corresponding to a 1.4% biaxial strain.[147] TERS has been used to study nanoscale defects and wrinkles on MoS_2 with a spatial resolution of ~ 18 nm, identifying localized inhomogeneities[148] and probing edge-related properties in few-layer MoS_2.[149]

More recently, the local doping variations in the depletion region in in-plane homojunctions in MoS_2 devices have been imaged using tip-enhanced photoluminescence (TEPL).[106] In TEPL, the local luminescence is measured rather than the phonon scattering, and Gadelha et al. used the spatial oscillation of the exciton and trion frequencies to image doping variations with nanometer resolution.

Other 2D materials have also been investigated by TERS, such as TMM gallium sulfide (GaS),[143] which is interesting for having two different Raman active A_{1g} modes. The authors reported that the phonon coherence length (L_c) for five-layer GaS is different for the A_{1g}^1 phonon ($L_c \sim 64$ nm) and for the A_{1g}^2 phonon ($L_c \sim 47$ nm). The L_c values were determined through

Fig. 9 (a) Giant gap-plasmon TERS on the TMD MoS_2 spectrum (left) on top of a substrate with gold nanodisks (right). The strong signals are recorded at the edges of the nanodisks.[142] (b) Tip-approach measurement that implies the spatial phonon length of the TMM GaS.[143] (c) Comparison of non-resonant (top) and resonant (bottom) TERS of TMD MoSe$_2$ and TERS image of the flake.[144] (d) TERS and TEPL spectra of the TMD WSe$_2$ as a function of the tip–sample distance.[145] Reproduced with permission from ref. 142–145.

23438 | *Phys. Chem. Chem. Phys.*, 2021, **23**, 23428–23444

This journal is © the Owner Societies 2021

the tip-approach experiment, which consists of moving the tip out from the sample at fixed steps and recording the Raman spectrum at each point, as displayed in Fig. 9(b) for the A_{1g}^1 peak. In order to do so, a curve must be fit to the experimental data that have L_c as one of its parameters, similarly to what was done in graphene.[111] As L_c becomes larger, so does the TERS enhancement. Additionally, they showed that L_c decreases as the number of layers decreases, suggesting that scattering with the surface of the substrate has a major role in the phonon decay process.

Back to TMDs, in monolayer MoSe$_2$, TERS has also been used to reveal nanoscale heterogeneities, by combining it with different scanning probe microscopy techniques.[144] Fig. 9(c) shows a non-resonant and a resonant TERS spectrum (top and bottom of Fig. 9(c), respectively). In the former, only one dominant peak at around 240 cm^{-1} (blue) is clearly distinguished, while in the latter there are other Raman peaks at 287 cm^{-1} (red) and 340 cm^{-1} (green). When comparing these measurements with α-MoO$_3$ TERS, it was possible to infer that these differences from non-resonant and resonant TERS spectra were due to the inclusion of MoO$_3$ in the MoSe$_2$ matrix.

In tungsten diselenide (WSe$_2$), TERS and TEPL nanospectroscopy and nanoimaging were combined, as shown in Fig. 9(d). Fig. 9(d) shows the Raman and PL spectra acquired at different tip–sample distances, showing the E$_{2g}$ (E′) and A$_{1g}$ $\left(A'_{1g}\right)$, respectively, at around 273 cm^{-1} and the first (150 cm^{-1}) and third (405 cm^{-1}) order LA phonons.[145] The authors also suggest that the shoulder in the TEPL spectra might have originated from the rise of trion or biexciton emissions. These features allowed the study of monolayer WSe$_2$ grown by physical vapor deposition of the associated nanoscale heterogeneities in the form of edges, grain boundaries and nucleation sites, extracting information about correlations of the photoluminescence spectral intensity, shifts with crystal edges and exciton diffusion length. The data suggest an approximately 25 nm exciton diffusion length, inferred to be due to the spatial scale of the photoluminescence quenching, and an around 30 to 80 nm wide region of optical heterogeneity at the edges. Still on WSe$_2$, it was also reported that other metals, besides Au and Ag, can be used to prepare a substrate for gap-mode TERS,[150] showing similar TERS measurement results for WSe$_2$ on Au and Cr substrates, implying that these results can be extended to other metals.

5 Summary and perspectives

In this article, we have reviewed recent results where different 2D materials were studied by CARS, SRS and TERS. These advanced techniques can overcome the two limitations of standard Raman spectroscopy, i.e. weak signal and low spatial resolution, providing a platform for advancing 2D materials' related science and also for the development of the techniques, having 2D materials as prototypes. The 2D systems are perfect surfaces and, therefore, a rich platform for experimental and theoretical developments, not only concerning the 2D science,

but also on the extremely important interaction of the material with the environment.

With the improved signal intensity provided by CARS and SRS, it has been shown that they provide fast Raman imaging, including in large electronic band gap materials (e.g. h-BN), which exhibit very low Raman signals due to the absence of resonant light–matter interactions. Technical improvements are still needed to measure 2D materials with more heavy atoms, due to their low frequency vibrational modes, hardly accessible in the stimulated regime utilized in CARS and SRS. For example, recent developments for performing SRS and CARS at low and THz frequency ranges[151,152] have been shown, and therefore they could be applied for imaging other 2D materials like TMDs, TMMs, black phosphorous and others. Moreover the ability to perform THz stimulated Raman imaging opens the opportunity to study not only phonons, but also other quasi-particles such as magnons in magnetic 2D materials.[153] Also, the applications of these techniques in heterostructures, including twisted homo- and hetero-bilayers, might also provide rich information. For example, it has been shown that low-frequency Raman modes arise in TMD heterostructures depending on the staking angle,[154,155] and therefore SRS and CARS can provide a fast imaging technique to probe the quality and staking order of these heterostructures.

Nano-Raman spectroscopy, as implemented here, based on the TERS effect, is mostly a surface technique and, in this sense, 2D materials represent a prototype for the study of the technique itself. Research about coherence in the near-field regime is in its early stage, with a clear impact of the use of nano-Raman to characterize materials, including the number of defects and local doping and strain of graphene deposited in different substrates. Besides the local study of doping, strain and defects, intentionally or unintentionally introduced in 2D samples and devices, the relevance of interaction with the environment, including contamination in the surface, e.g. a commonly found surface water layer, among others, is a subject to be explored. The tip-approach procedure has been shown to be a unique technique to get information about symmetry and nano-meter sized coherence length for phonon mediated scattering. However, related studies are still limited to two cases (graphene and GaS) and more experimental and theoretical work is needed to fully understand the related effects and how it applies to other 2D materials. The nano-Raman spatial resolution and antenna enhancement properties are still under debate, and here, again, 2D materials might also represent a valuable reference system.[156] With these aspects clearly established, nano-Raman can become an odd technique for nanometrology, not only for 2D-systems,[157] but back to more complex nano-materials where rich Raman behavior has been observed.[158] Besides, most 2D materials from different classes, such as h-BN, phosphorene and many others, are still untouched by the technique.

One potentially important application of nano-Raman is in the twistronics field, where novel phenomena are observed due to potentials fluctuating in the nano-scale. The twist between two 2D layers has been shown to generate interesting results in

homo-bilayers, using two identical layers of different 2D materials,[124,159] and also in hetero-bilayers,[160] where two different layered materials are stacked together. Notably, a new field emerged, named twistronics, where TBG has been shown to exhibit ferromagnetism[64] in a quantum Chern insulator,[161] large linear-in-temperature resistivity,[162] nematicity,[163] plasmonic collective excitation[164] and tunable photonic crystals[125] and, more recently, the localization of lattice phenomena, such as electrons and phonons,[93] and the photothermoelectric effect.[126] Moreover, interesting effects were observed or predicted in twisted heterostructures of TMDs, such as correlated electronic phases in twisted homo-bilayers of WSe2,[165] the prediction of localized excitons in twisted homo-bilayers of MoS_2,[166] and evidence for moiré excitons in hetero-bilayers of MoSe2/WSe2.[160] However, to access moiré pattern related physics, spatial resolution might be a problem. The increased optical resolution in TERS experiments allows the collection of information about defects and phonon coherence length and imaging of moiré patters that is not possible using far-field Raman spectroscopy.

Finally, the combination of TERS with CARS or SRS has the potential to generate high-resolution, information-rich and fast Raman spectral imaging. Given the relevance of Raman spectroscopy as a tool for materials characterization, we believe that this is an important subject for future studies in nanometrology.

Conflicts of interest

The authors declare no conflicts of interest.

Acknowledgements

Notes and references

1 L. Malard, M. Pimenta, G. Dresselhaus and M. Dresselhaus, *Phys. Rep.*, 2009, **473**, 51–87.

2 M. S. Dresselhaus, A. Jorio, M. Hofmann, G. Dresselhaus and R. Saito, *Nano Lett.*, 2010, **10**, 751–758.

3 R. Saito, M. Hofmann, G. Dresselhaus, A. Jorio and M. Dresselhaus, *Adv. Phys.*, 2011, **60**, 413–550.

4 A. Jorio, M. S. Dresselhaus, R. Saito and G. Dresselhaus, *Raman spectroscopy in graphene related systems*, John Wiley & Sons, 2011.

5 M. A. Pimenta, G. Dresselhaus, M. S. Dresselhaus, L. G. Cançado, A. Jorio and R. Saito, *Phys. Chem. Chem. Phys.*, 2007, **9**, 1276–1290.

6 J. N. Coleman, M. Lotya, A. ONeill, S. D. Bergin, P. J. King, U. Khan, K. Young, A. Gaucher, S. De and R. J. Smith, *et al.*, *Science*, 2011, **331**, 568–571.

7 A. C. Ferrari and D. M. Basko, *Nat. Nanotechnol.*, 2013, **8**, 235–246.

8 S. Z. Butler, S. M. Hollen, L. Cao, Y. Cui, J. A. Gupta, H. R. Gutiérrez, T. F. Heinz, S. S. Hong, J. Huang and A. F. Ismach, *et al.*, *ACS Nano*, 2013, **7**, 2898–2926.

9 M. A. Pimenta, E. del Corro, B. R. Carvalho, C. Fantini and L. M. Malard, *Acc. Chem. Res.*, 2015, **48**, 41–47.

10 G. R. Bhimanapati, Z. Lin, V. Meunier, Y. Jung, J. Cha, S. Das, D. Xiao, Y. Son, M. S. Strano and V. R. Cooper, *et al.*, *ACS Nano*, 2015, **9**, 11509–11539.

11 R. Saito, Y. Tatsumi, S. Huang, X. Ling and M. S. Dresselhaus, *J. Phys.: Condens. Matter*, 2016, **28**, 353002.

12 P.-H. Tan, *Raman Spectroscopy of two-dimensional materials*, Springer, 2018, vol. 276.

13 X. Cong, X.-L. Liu, M.-L. Lin and P.-H. Tan, *npj 2D Mater. Appl.*, 2020, **4**, 1–12.

14 H. B. Ribeiro, M. A. Pimenta and C. J. de Matos, *J. Raman Spectrosc.*, 2018, **49**, 76–90.

15 A. C. Ferrari, J. C. Meyer, V. Scardaci, C. Casiraghi, M. Lazzeri, F. Mauri, S. Piscanec, D. Jiang, K. S. Novoselov and S. Roth, *et al.*, *Phys. Rev. Lett.*, 2006, **97**, 187401.

16 H. Li, Q. Zhang, C. C. R. Yap, B. K. Tay, T. H. T. Edwin, A. Olivier and D. Baillargeat, *Adv. Funct. Mater.*, 2012, **22**, 1385–1390.

17 B. Chakraborty, H. R. Matte, A. Sood and C. Rao, *J. Raman Spectrosc.*, 2013, **44**, 92–96.

18 L. Cançado, K. Takai, T. Enoki, M. Endo, Y. Kim, H. Mizusaki, N. Speziali, A. Jorio and M. Pimenta, *Carbon*, 2008, **46**, 272–275.

19 J. Ribeiro-Soares, R. Almeida, E. B. Barros, P. T. Araujo, M. S. Dresselhaus, L. G. Cançado and A. Jorio, *Phys. Rev. B: Condens. Matter Mater. Phys.*, 2014, **90**, 115438.

20 J. Ribeiro-Soares, R. Almeida, L. G. Cançado, M. S. Dresselhaus and A. Jorio, *Phys. Rev. B: Condens. Matter Mater. Phys.*, 2015, **91**, 205421.

21 L. G. Cançado, M. A. Pimenta, B. R. A. Neves, M. S. S. Dantas and A. Jorio, *Phys. Rev. Lett.*, 2004, **93**, 247401.

22 C. Casiraghi, A. Hartschuh, H. Qian, S. Pliscanec, C. Georgia, A. Fasoli, K. Novoselov, D. Basko and A. Ferrari, *Nano Lett.*, 2009, **9**, 1433–1441.

23 H. B. Ribeiro, M. A. Pimenta, C. J. S. de Matos, R. L. Moreira, A. S. Rodin, J. D. Zapata, E. A. T. de Souza and A. H. Castro Neto, *ACS Nano*, 2015, **9**, 4270–4276.

24 C. Lee, H. Yan, L. E. Brus, T. F. Heinz, J. Hone and S. Ryu, *ACS Nano*, 2010, **4**, 2695–2700.

25 L. G. Cançado, M. G. Da Silva, E. H. M. Ferreira, F. Hof, K. Kampioti, K. Huang, A. Pénicaud, C. A. Achete, R. B. Capaz and A. Jorio, *2D Mater.*, 2017, **4**, 025039.

26 S. Pisana, M. Lazzeri, C. Casiraghi, K. S. Novoselov, A. K. Geim, A. C. Ferrari and F. Mauri, *Nat. Mater.*, 2007, **6**, 198–201.

27 J. Yan, Y. Zhang, P. Kim and A. Pinczuk, *Phys. Rev. Lett.*, 2007, **98**, 166802.

28 A. Das, S. Pisana, B. Chakraborty, S. Piscanec, S. K. Saha, U. V. Waghmare, K. S. Novoselov, H. R. Krishnamurthy, A. K. Geim, A. C. Ferrari and A. K. Sood, *Nat. Nanotechnol.*, 2008, **3**, 210–215.

29 R. Beams, L. G. Cançado and L. Novotny, *J. Phys.: Condens. Matter*, 2015, **27**, 083002.

30 K. N. Kudin, B. Ozbas, H. C. Schniepp, R. K. Prud'Homme, I. A. Aksay and R. Car, *Nano Lett.*, 2008, **8**, 36–41.

31 P. Vecera, J. C. Chacón-Torres, T. Pichler, S. Reich, H. R. Soni, A. Görling, K. Edelthalhammer, H. Peterlik, F. Hauke and A. Hirsch, *Nat. Commun.*, 2017, **8**, 1–9.

32 T. M. G. Mohiuddin, A. Lombardo, R. R. Nair, A. Bonetti, G. Savini, R. Jalil, N. Bonini, D. M. Basko, C. Galiotis, N. Marzari, K. S. Novoselov, A. K. Geim and A. C. Ferrari, *Phys. Rev. B: Condens. Matter Mater. Phys.*, 2009, **79**, 205433.

33 B. Pettinger, B. Ren, G. Picardi, R. Schuster and G. Ertl, *Phys. Rev. Lett.*, 2004, **92**, 096101.

34 Y.-T. Li, L.-L. Qu, D.-W. Li, Q.-X. Song, F. Fathi and Y.-T. Long, *Biosens. Bioelectron.*, 2013, **43**, 94–100.

35 S. Feng, M. C. Dos Santos, B. R. Carvalho, R. Lv, Q. Li, K. Fujisawa, A. L. Elas, Y. Lei, N. Perea-López and M. Endo, *et al.*, *Sci. Adv.*, 2016, **2**, e1600322.

36 S. A. Ghopry, S. M. Sadeghi, Y. Farhat, C. L. Berrie, M. Alamri and J. Z. Wu, *ACS Appl. Nano Mater.*, 2021, **4**, 2941–2951.

37 H. Malekpour and A. A. Balandin, *J. Raman Spectrosc.*, 2018, **49**, 106–120.

38 S. Sahoo, A. P. Gaur, M. Ahmadi, M. J.-F. Guinel and R. S. Katiyar, *J. Phys. Chem. C*, 2013, **117**, 9042–9047.

39 R. R. Jones, D. C. Hooper, L. Zhang, D. Wolverson and V. K. Valev, *Nanoscale Res. Lett.*, 2019, **14**, 231.

40 R. W. Boyd, *Nonlinear Optics*, Academic Press, 3rd edn, 2008.

41 J.-X. Cheng and X. S. Xie, *Coherent Raman Scattering Microscopy*, CRC Press, Boca Raton, FL, 2013.

42 L. Novotny and B. Hecht, *Principles of Nano-Optics*, Cambridge university press, 2012.

43 V. N. Popov and P. Lambin, *Phys. Rev. B*, 2006, **73**, 085407.

44 Q. Cai, D. Scullion, A. Falin, K. Watanabe, T. Taniguchi, Y. Chen, E. J. G. Santos and L. H. Li, *Nanoscale*, 2017, **9**, 3059–3067.

45 A. Molina-Sánchez and L. Wirtz, *Phys. Rev. B: Condens. Matter Mater. Phys.*, 2011, **84**, 155413.

46 H. Wang, G. Qin, J. Yang, Z. Qin, Y. Yao, Q. Wang and M. Hu, *J. Appl. Phys.*, 2019, **125**, 245104.

47 M. S. Dresselhaus, G. Dresselhaus and A. Jorio, *Group theory: application to the physics of condensed matter*, Springer Science & Business Media, 2007.

48 L. M. Malard, M. H. Guimarães, D. L. Mafra and A. Jorio, *et al.*, *Phys. Rev. B: Condens. Matter Mater. Phys.*, 2009, **79**, 125426.

49 R. Alencar, R. Longuinhos, C. Rabelo, H. Miranda, B. Viana, A. Souza Filho, L. Cançado, A. Jorio and J. Ribeiro-Soares, *Phys. Rev. B*, 2020, **102**, 165307.

50 R. Boyd, *Nonlinear Optics*, Academic Press, London, 2008.

51 B. Sharma, R. R. Frontiera, A.-I. Henry, E. Ringe and R. P. Van Duyne, *Mater. today*, 2012, **15**, 16–25.

52 S.-Y. Ding, J. Yi, J.-F. Li, B. Ren, D.-Y. Wu, R. Panneerselvam and Z.-Q. Tian, *Nat. Rev. Mater.*, 2016, **1**, 1–16.

53 J. Langer, D. Jimenez de Aberasturi, J. Aizpurua, R. A. Alvarez-Puebla, B. Auguié, J. J. Baumberg, G. C. Bazan, S. E. Bell, A. Boisen and A. G. Brolo, *et al.*, *ACS Nano*, 2019, **14**, 28–117.

54 Y.-R. Shen, *The Principles of Nonlinear Optics*, Wiley-Interscience, New York, 2003.

55 L. M. Malard, T. V. Alencar, A. P. M. Barboza, K. F. Mak and A. M. de Paula, *Phys. Rev. B: Condens. Matter Mater. Phys.*, 2013, **87**, 201401.

56 N. Kumar, S. Najmaei, Q. Cui, F. Ceballos, P. M. Ajayan, J. Lou and H. Zhao, *Phys. Rev. B: Condens. Matter Mater. Phys.*, 2013, **87**, 161403.

57 Y. Li, Y. Rao, K. F. Mak, Y. You, S. Wang, C. R. Dean and T. F. Heinz, *Nano Lett.*, 2013, **13**, 3329–3333.

58 X. Yin, Z. Ye, D. A. Chenet, Y. Ye, K. O'Brien, J. C. Hone and X. Zhang, *Science*, 2014, **344**, 488–490.

59 W.-T. Hsu, Z.-A. Zhao, L.-J. Li, C.-H. Chen, M.-H. Chiu, P.-S. Chang, Y.-C. Chou and W.-H. Chang, *ACS Nano*, 2014, **8**, 2951–2958.

60 X. Zhou, J. Cheng, Y. Zhou, T. Cao, H. Hong, Z. Liao, S. Wu, H. Peng, K. Liu and D. Yu, *J. Am. Chem. Soc.*, 2015, **137**, 7994–7997.

61 J. Ribeiro-Soares, C. Janisch, Z. Liu, A. L. Elias, M. S. Dresselhaus, M. Terrones, L. G. Cançado and A. Jorio, *2D Mater.*, 2015, **2**, 045015.

62 R. Beams, L. G. Cançado, S. Krylyuk, I. Kalish, B. C. Kalanyan, A. K. Singh, K. Choudhary, A. Bruma, P. M. Vora, F. Tavazza, A. V. Davydov and S. J. Stranick, *ACS Nano*, 2016, **10**, 9626–9636.

63 L. Lafeta, A. Corradi, T. Zhang, E. Kahn, I. Bilgin, B. R. Carvalho, S. Kar, M. Terrones and L. M. Malard, *2D Mater.*, 2021, **8**, 035010.

64 W. Kim, J. Y. Ahn, J. Oh, J. H. Shim and S. Ryu, *Nano Lett.*, 2020, **20**, 8825–8831.

65 B. R. Carvalho, Y. Wang, K. Fujisawa, T. Zhang, E. Kahn, I. Bilgin, P. M. Ajayan, A. M. de Paula, M. A. Pimenta, S. Kar, V. H. Crespi, M. Terrones and L. M. Malard, *Nano Lett.*, 2020, **20**, 284–291.

66 H. Ma, J. Liang, H. Hong, K. Liu, D. Zou, M. Wu and K. Liu, *Nanoscale*, 2020, **12**, 22891–22903.

67 A. Autere, H. Jussila, A. Marini, J. Saavedra, Y. Dai, A. Säynätjoki, L. Karvonen, H. Yang, B. Amirsolaimani and R. A. Norwood, *et al.*, *Phys. Rev. B*, 2018, **98**, 115426.

68 J. L. Suhalim, J. C. Boik, B. J. Tromberg and E. O. Potma, *J. Biophotonics*, 2012, **5**, 387–395.

69 E. Singe, *Philos. Mag.*, 1928, **6**, 356.

70 G. Tarrach, M. Bopp, D. Zeisel and A. Meixner, *Rev. Sci. Instrum.*, 1995, **66**, 3569–3575.

71 L. Novotny, *Progress Opt.*, 2007, **50**, 137.

72 M. D. Costa, L. G. Cançado and A. Jorio, *J. Raman Spectrosc.*, 2021, **52**, 587–588.

73 R. M. Stöckle, Y. D. Suh, V. Deckert and R. Zenobi, *Chem. Phys. Lett.*, 2000, **318**, 131–136.

74 N. Hayazawa, Y. Inouye, Z. Sekkat and S. Kawata, *Opt. Commun.*, 2000, **183**, 333–336.

This journal is © the Owner Societies 2021

Phys. Chem. Chem. Phys., 2021, **23**, 23428–23444 | **23441**

75 L. G. Cançado, A. Hartschuh and L. Novotny, *J. Raman Spectrosc.*, 2009, **40**, 1420–1426.

76 B.-S. Yeo, J. Stadler, T. Schmid, R. Zenobi and W. Zhang, *Chem. Phys. Lett.*, 2009, **472**, 1–13.

77 J. Stadler, T. Schmid and R. Zenobi, *Nanoscale*, 2012, **4**, 1856–1870.

78 L. Langelüddecke, P. Singh and V. Deckert, *Appl. Spectrosc.*, 2015, **69**, 1357–1371.

79 T. Deckert-Gaudig, A. Taguchi, S. Kawata and V. Deckert, *Chem. Soc. Rev.*, 2017, **46**, 4077–4110.

80 F. Shao and R. Zenobi, *Anal. Bioanal. Chem.*, 2019, **411**, 37–61.

81 N. Mauser and A. Hartschuh, *Chem. Soc. Rev.*, 2014, **43**, 1248–1262.

82 X. Shi, N. Coca-López, J. Janik and A. Hartschuh, *Chem. Rev.*, 2017, **117**, 4945–4960.

83 C. Rabelo, H. Miranda, T. L. Vasconcelos, L. G. Cançado and A. Jorio, 2019 4th International Symposium on Instrumentation Systems, Circuits and Transducers (INSCIT), 2019, pp. 1-6.

84 H. Miranda, C. Rabelo, T. L. Vasconcelos, L. G. Cançado and A. Jorio, 2019 4th International Symposium on Instrumentation Systems, Circuits and Transducers (INSCIT), 2019, pp. 1-5.

85 H. Miranda, C. Rabelo, L. G. Cançado, T. L. Vasconcelos, B. S. Oliveira, F. Schulz, H. Lange, S. Reich, P. Kusch and A. Jorio, *Phys. Rev. Res.*, 2020, **2**, 023408.

86 R. V. Maximiano, R. Beams, L. Novotny, A. Jorio and L. G. Cançado, *Phys. Rev. B: Condens. Matter Mater. Phys.*, 2012, **85**, 235434.

87 B. Ren, G. Picardi and B. Pettinger, *Rev. Sci. Instrum.*, 2004, **75**, 837–841.

88 P. Muehlschlegel, H.-J. Eisler, O. J. Martin, B. Hecht and D. Pohl, *Science*, 2005, **308**, 1607–1609.

89 L. Novotny and N. Van Hulst, *Nat. Photonics*, 2011, **5**, 83–90.

90 T. L. Vasconcelos, B. S. Archanjo, B. S. Oliveira, R. Valaski, R. C. Cordeiro, H. G. Medeiros, C. Rabelo, A. Ribeiro, P. Ercius, C. A. Achete, A. Jorio and L. G. Cançado, *Adv. Opt. Mater.*, 2018, **6**, 1800528.

91 T. L. Vasconcelos, B. S. Archanjo, B. S. Oliveira, W. F. Silva, R. S. Alencar, C. Rabelo, C. A. Achete, A. Jorio and L. G. Cançado, *IEEE J. Sel. Top. Quantum Electron.*, 2020, **27**, 1–11.

92 H. Miranda, C. Rabelo, T. L. Vasconcelos, L. G. Cançado and A. Jorio, *Phys. Status Solidi RRL*, 2020, **14**, 2000212.

93 A. C. Gadelha, D. A. Ohlberg, C. Rabelo, E. G. Neto, T. L. Vasconcelos, J. L. Campos, J. S. Lemos, V. Ornelas, D. Miranda and R. Nadas, *et al.*, *Nature*, 2021, **590**, 405–409.

94 L. Lafetá, A. R. Cadore, T. G. Mendes-de Sa, K. Watanabe, T. Taniguchi, L. C. Campos, A. Jorio and L. M. Malard, *Nano Lett.*, 2017, **17**, 3447–3451.

95 A. Virga, C. Ferrante, G. Batignani, D. De Fazio, A. Nunn, A. Ferrari, G. Cerullo and T. Scopigno, *Nat. Commun.*, 2019, **10**, 1–9.

96 A. Paddubskaya, D. Rutkauskas, R. Karpicz, G. Dovbeshko, N. Nebogatikova, I. Antonova and A. Dementjev, *Nanoscale Res. Lett.*, 2020, **15**, 37.

97 E. Hendry, P. J. Hale, J. Moger, A. K. Savchenko and S. A. Mikhailov, *Phys. Rev. Lett.*, 2010, **105**, 097401.

98 E. O. Potma and S. Mukamel, *Coherent Raman Scattering Microscopy*, 2012, pp. 3–42.

99 A. Jorio, G. Dresselhaus and M. S. Dresselhaus, *Carbon nanotubes: advanced topics in the synthesis, structure, properties and applications*, Springer Science & Business Media, 2007, vol. 111.

100 L. G. Cançado, R. Beams, A. Jorio and L. Novotny, *Phys. Rev. X*, 2014, **4**, 031054.

101 C. Rabelo, T. L. Vasconcelos, B. C. Publio, H. Miranda, L. G. Cançado and A. Jorio, *Phys. Rev. Appl.*, 2020, **14**, 024056.

102 A. Hartschuh, E. J. Sánchez, X. S. Xie and L. Novotny, *Phys. Rev. Lett.*, 2003, **90**, 095503.

103 N. Hayazawa, T. Yano, H. Watanabe, Y. Inouye and S. Kawata, *Chem. Phys. Lett.*, 2003, **376**, 174–180.

104 I. O. Maciel, N. Anderson, M. A. Pimenta, A. Hartschuh, H. Qian, M. Terrones, H. Terrones, J. Campos-Delgado, A. M. Rao and L. Novotny, *et al.*, *Nat. Mater.*, 2008, **7**, 878–883.

105 R. Kato, S. Igarashi, T. Umakoshi and P. Verma, *ACS Appl. Nano Mater.*, 2020, **3**(6), 6001–6008.

106 A. C. Gadelha, T. L. Vasconcelos, L. G. Cançado and A. Jorio, *J. Phys. Chem. Lett.*, 2021, **12**, 7625–7631.

107 R. Beams, L. G. Cançado, A. Jorio, A. N. Vamivakas and L. Novotny, *Nanotechnology*, 2015, **26**, 175702.

108 A. C. Gadelha, D. A. Ohlberg, F. C. Santana, G. S. Eliel, J. S. Lemos, V. Ornelas, D. Miranda, R. B. Nadas, K. Watanabe and T. Taniguchi, *et al.*, *ACS Appl. Nano Mater.*, 2021, **4**, 1858–1866.

109 R. Beams, *J. Raman Spectrosc.*, 2018, **49**, 157–167.

110 A. Jorio, N. S. Mueller and S. Reich, *Phys. Rev. B*, 2017, **95**, 155409.

111 R. Beams, L. G. Cançado, S.-H. Oh, A. Jorio and L. Novotny, *Phys. Rev. Lett.*, 2014, **113**, 186101.

112 J. Ribeiro-Soares, M. Oliveros, C. Garin, M. David, L. Martins, C. Almeida, E. Martins-Ferreira, K. Takai, T. Enoki, R. Magalhães-Paniago, A. Malachias, A. Jorio, B. Archanjo, C. Achete and L. G. Cançado, *Carbon*, 2015, **95**, 646–652.

113 W. Carter and E. Wolf, *JOSA*, 1975, **65**, 1067–1071.

114 W. Hayes and R. Loudon, *Scattering of light by crystals*, Courier Corporation, 2012.

115 L. Cançado, A. Jorio, A. Ismach, E. Joselevich, A. Hartschuh and L. Novotny, *Phys. Rev. Lett.*, 2009, **103**, 186101.

116 F. D. V. Araujo, V. V. Oliveira, A. C. Gadelha, T. C. V. Carvalho, T. F. D. Fernandes, F. W. N. Silva, R. Longuinhos, J. Ribeiro Soares, A. Jorio and A. G. Souza Filho, *Nanotechnology*, 2020, **31**(49), 495702.

117 M. Lucchese, F. Stavale, E. M. Ferreira, C. Vilani, M. Moutinho, R. B. Capaz, C. Achete and A. Jorio, *Carbon*, 2010, **48**, 1592–1597.

118 R. Beams, L. G. Cançado and L. Novotny, *Nano Lett.*, 2011, **11**, 1177–1181.

119 L. G. Cançado, A. Jorio, E. M. Ferreira, F. Stavale, C. A. Achete, R. B. Capaz, M. V. D. O. Moutinho, A. Lombardo, T. Kulmala and A. C. Ferrari, *Nano Lett.*, 2011, **11**, 3190–3196.

120 L. Cançado, K. Takai, T. Enoki, M. Endo, Y. Kim, H. Mizusaki, A. Jorio, L. Coelho, R. Magalhaes-Paniago and M. Pimenta, *Appl. Phys. Lett.*, 2006, **88**, 163106.

121 Y. Cao, V. Fatemi, S. Fang, K. Watanabe, T. Taniguchi, E. Kaxiras and P. Jarillo-Herrero, *Nature*, 2018, **556**, 43–50.

122 Y. Cao, V. Fatemi, A. Demir, S. Fang, S. L. Tomarken, J. Y. Luo, J. D. Sanchez-Yamagishi, K. Watanabe, T. Taniguchi, E. Kaxiras, R. C. Ashoori and P. Jarillo-Herrero, *Nature*, 2018, **556**, 80–84.

123 H. Yoo, R. Engelke, S. Carr, S. Fang, K. Zhang, P. Cazeaux, S. H. Sung, R. Hovden, A. W. Tsen, T. Taniguchi, K. Watanabe, G.-C. Yi, M. Kim, M. Luskin, E. B. Tadmor, E. Kaxiras and P. Kim, *Nat. Mater.*, 2019, **18**, 448–453.

124 A. Weston, Y. Zou, V. Enaldiev, A. Summerfield, N. Clark, V. Zólyomi, A. Graham, C. Yelgel, S. Magorrian, M. Zhou, J. Zultak, D. Hopkinson, A. Barinov, T. H. Bointon, A. Kretinin, N. R. Wilson, P. H. Beton, V. I. Falko, S. J. Haigh and R. Gorbachev, *Nat. Nanotechnol.*, 2020, **15**, 592–597.

125 S. S. Sunku, G. X. Ni, B. Y. Jiang, H. Yoo, A. Sternbach, A. S. McLeod, T. Stauber, L. Xiong, T. Taniguchi, K. Watanabe, P. Kim, M. M. Fogler and D. N. Basov, *Science*, 2018, **362**, 1153–1156.

126 S. S. Sunku, D. Halbertal, T. Stauber, S. Chen, A. S. McLeod, A. Rikhter, M. E. Berkowitz, C. F. B. Lo, D. E. Gonzalez-Acevedo, J. C. Hone, C. R. Dean, M. M. Fogler and D. N. Basov, *Nat. Commun.*, 2021, **12**, 1641.

127 N. C. H. Hesp, I. Torre, D. Barcons-Ruiz, H. Herzig Shein-fux, K. Watanabe, T. Taniguchi, R. Krishna Kumar and F. H. L. Koppens, *Nat. Commun.*, 2021, **12**, 1640.

128 T.-F. Chung, R. He, T.-L. Wu and Y. P. Chen, *Nano Lett.*, 2015, **15**, 1203–1210.

129 M. Lamparski, B. Van Troeye and V. Meunier, *2D Mater.*, 2020, **7**, 025050.

130 V.-H. Nguyen, D. Paszko, M. Lamparski, B. Van Troeye, V. Meunier and J.-C. Charlier, *2D Mater.*, 2021, **8**, 035046.

131 Y. Xie, B. Lian, B. Jäck, X. Liu, C.-L. Chiu, K. Watanabe, T. Taniguchi, B. A. Bernevig and A. Yazdani, *Nature*, 2019, **572**, 101–105.

132 R. V. Gorbachev, I. Riaz, R. R. Nair, R. Jalil, L. Britnell, B. D. Belle, E. W. Hill, K. S. Novoselov, K. Watanabe, T. Taniguchi, A. K. Geim and P. Blake, *Small*, 2011, **7**, 465–468.

133 J.-X. Cheng and X. S. Xie, *Science*, 2015, **350**, aaa8870.

134 F. Hu, L. Shi and W. Min, *Nat. Methods*, 2019, **16**, 830–842.

135 R. Cunha, L. Lafeta, E. A. Fonseca, A. Barbosa, M. A. Romano-Silva, R. Vieira, A. Jorio and L. M. Malard, *Analyst*, 2021, **146**, 2945–2954.

136 J. Ling, X. Miao, Y. Sun, Y. Feng, L. Zhang, Z. Sun and M. Ji, *ACS Nano*, 2019, **13**, 14033–14040.

137 Y. Gao, W. Ren, T. Ma, Z. Liu, Y. Zhang, W.-B. Liu, L.-P. Ma, X. Ma and H.-M. Cheng, *ACS Nano*, 2013, **7**, 5199–5206.

138 L. H. Li, J. Cervenka, K. Watanabe, T. Taniguchi and Y. Chen, *ACS Nano*, 2014, **8**, 1457–1462.

139 L. H. Li, E. J. G. Santos, T. Xing, E. Cappelluti, R. Roldán, Y. Chen, K. Watanabe and T. Taniguchi, *Nano Lett.*, 2015, **15**, 218–223.

140 Q. Cai, L. H. Li, Y. Yu, Y. Liu, S. Huang, Y. Chen, K. Watanabe and T. Taniguchi, *Phys. Chem. Chem. Phys.*, 2015, **17**, 7761–7766.

141 B. A. Ko, A. V. Sokolov, M. O. Scully, Z. Zhang and H. W. H. Lee, *Photonics Res.*, 2019, **7**, 251–259.

142 A. G. Milekhin, M. Rahaman, E. E. Rodyakina, A. V. Latyshev, V. M. Dzhagan and D. R. Zahn, *Nanoscale*, 2018, **10**, 2755–2763.

143 R. Alencar, C. Rabelo, H. L. Miranda, T. L. Vasconcelos, B. S. Oliveira, A. Ribeiro, B. C. Publio, J. Ribeiro-Soares, A. S. Filho and L. G. Cançado, *et al.*, *Nano Lett.*, 2019, **19**, 7357–7364.

144 K. K. Smithe, A. V. Krayev, C. S. Bailey, H. R. Lee, E. Yalon, O. B. Aslan, M. Muñoz Rojo, S. Krylyuk, P. Taheri and A. V. Davydov, *et al.*, *ACS Appl. Nano Mater.*, 2018, **1**, 572–579.

145 K.-D. Park, O. Khatib, V. Kravtsov, G. Clark, X. Xu and M. B. Raschke, *Nano Lett.*, 2016, **16**, 2621–2627.

146 W. Su, N. Kumar, S. Mignuzzi, J. Crain and D. Roy, *Nanoscale*, 2016, **8**, 10564–10569.

147 M. Rahaman, R. D. Rodriguez, G. Plechinger, S. Moras, C. Schüller, T. Korn and D. R. Zahn, *Nano Lett.*, 2017, **17**, 6027–6033.

148 R. Kato, T. Umakoshi, R. T. Sam and P. Verma, *Appl. Phys. Lett.*, 2019, **114**, 073105.

149 T.-X. Huang, X. Cong, S.-S. Wu, K.-Q. Lin, X. Yao, Y.-H. He, J.-B. Wu, Y.-F. Bao, S.-C. Huang and X. Wang, *et al.*, *Nat. Commun.*, 2019, **10**, 1–8.

150 A. Krayev, S. Krylyuk, R. Ilic, A. R. Hight Walker, A. Bhattarai, A. G. Joly, M. Velický, A. V. Davydov and P. Z. El-Khoury, *J. Phys. Chem. C*, 2020, **124**, 8971–8977.

151 L. Ren, I. Hurwitz, D. Raanan, P. Oulevey, D. Oron and Y. Silberberg, *Optica*, 2019, **6**, 52–55.

152 Y. Soffer, D. Raanan and D. Oron, *ACS Photonics*, 2020, **7**, 3481–3488.

153 M. Gibertini, M. Koperski, A. F. Morpurgo and K. S. Novoselov, *Nat. Nanotechnol.*, 2019, **14**, 408–419.

154 K.-Q. Lin, J. Holler, J. M. Bauer, P. Parzefall, M. Scheuck, B. Peng, T. Korn, S. Bange, J. M. Lupton and C. Schüller, *Adv. Mater.*, 2021, **33**, 2008333.

155 J. Quan, L. Linhart, M.-L. Lin, D. Lee, J. Zhu, C.-Y. Wang, W.-T. Hsu, J. Choi, J. Embley, C. Young, T. Taniguchi, K. Watanabe, C.-K. Shih, K. Lai, A. H. MacDonald, P.-H. Tan, F. Libisch and X. Li, *Nat. Mater.*, 2021, **20**, 1100–1105.

156 A. R. Neto, C. Rabelo, L. G. Cançado, M. Engel, M. Steiner and A. Jorio, 2019 4th International Symposium on Instrumentation Systems, Circuits and Transducers (INSCIT), 2019, pp. 1-6.

This journal is © the Owner Societies 2021

Phys. Chem. Chem. Phys., 2021, **23**, 23428–23444 | **23443**

157 D. L. Silva, J. L. E. Campos, T. F. Fernandes, J. N. Rocha, L. R. Machado, E. M. Soares, D. R. Miquita, H. Miranda, C. Rabelo and O. P. V. Neto, *et al.*, *Carbon*, 2020, **161**, 181–189.

158 R. Kumar, H. K. Choudhary, S. P. Pawar, S. Bose and B. Sahoo, *Phys. Chem. Chem. Phys.*, 2017, **19**, 23268–23279.

159 M. Liao, Z. Wei, L. Du, Q. Wang, J. Tang, H. Yu, F. Wu, J. Zhao, X. Xu, B. Han, K. Liu, P. Gao, T. Polcar, Z. Sun, D. Shi, R. Yang and G. Zhang, *Nat. Commun.*, 2020, **11**, 2153.

160 K. Tran, G. Moody, F. Wu, X. Lu, J. Choi, K. Kim, A. Rai, D. A. Sanchez, J. Quan, A. Singh, J. Embley, A. Zepeda, M. Campbell, T. Autry, T. Taniguchi, K. Watanabe, N. Lu, S. K. Banerjee, K. L. Silverman, S. Kim, E. Tutuc, L. Yang, A. H. MacDonald and X. Li, *Nature*, 2019, **567**, 71–75.

161 K. P. Nuckolls, M. Oh, D. Wong, B. Lian, K. Watanabe, T. Taniguchi, B. A. Bernevig and A. Yazdani, *Nature*, 2020, **588**, 610–615.

162 H. Polshyn, M. Yankowitz, S. Chen, Y. Zhang, K. Watanabe, T. Taniguchi, C. R. Dean and A. F. Young, *Nat. Phys.*, 2019, **15**, 1011–1016.

163 Y. Cao, D. Rodan-Legrain, J. M. Park, N. F. Q. Yuan, K. Watanabe, T. Taniguchi, R. M. Fernandes, L. Fu and P. Jarillo-Herrero, *Science*, 2021, **372**, 264–271.

164 N. C. H. Hesp, I. Torre, D. Rodan-Legrain, P. Novelli, Y. Cao, S. Carr, S. Fang, P. Stepanov, D. Barcons-Ruiz, H. Herzig-Sheinfux, K. Watanabe, T. Taniguchi, D. K. Efetov, E. Kaxiras, P. Jarillo-Herrero, M. Polini and F. H. L. Koppens, *Collective excitations in twisted bilayer graphene close to the magic angle*, 2019.

165 L. Wang, E.-M. Shih, A. Ghiotto, L. Xian, D. A. Rhodes, C. Tan, M. Claassen, D. M. Kennes, Y. Bai, B. Kim, K. Watanabe, T. Taniguchi, X. Zhu, J. Hone, A. Rubio, A. N. Pasupathy and C. R. Dean, *Nat. Mater.*, 2020, **19**, 861–866.

166 S. Venkateswarlu, A. Honecker and G. Trambly de Laissardière, *Phys. Rev. B*, 2020, **102**, 081103.